

# Enhancing GNSS Water Vapour Retrieval via Synergistic Microwave Radiometry: Thermodynamic Error Diagnosis and Bias Correction

Avinash N. Parde<sup>1</sup>, Christina Oikonomou<sup>1</sup>, Haris Haralambous<sup>1,2</sup>

<sup>1</sup>Frederick Research Center, Nicosia, 1036, Cyprus

<sup>2</sup>Frederick University, Nicosia, 1036, Cyprus

**Correspondence:** Avinash N. Parde ([res.pav@frederick.ac.cy](mailto:res.pav@frederick.ac.cy))

## Abstract.

The retrieval of Precipitable Water Vapour (PWV) from Global Navigation Satellite Systems (GNSS) in thermodynamically complex environments is significantly limited by the accuracy of the weighted mean temperature ( $T_m$ ). This study evaluates the efficacy of static climatological models versus dynamic ground-based microwave radiometry for  $T_m$  determination in the Eastern Mediterranean, a region characterized by sharp refractivity gradients. Using the Cyprus GNSS Meteorology Enhancement research project (CYGMEN) infrastructure in Nicosia, the performance of the ERA5-based HGPT2 model and a co-located Microwave Radiometer (MWR) was assessed against radiosonde (RS) profiles during the 2025 warm season (Spring–Summer). Diagnostic analysis reveals that the static HGPT2 model fails to resolve the diurnal thermodynamic decoupling between the boundary layer and the free troposphere, leading to a systematic overestimation of  $T_m$  exceeding 6 K during peak solar insolation. Conversely, the MWR captures short-term thermodynamic variability ( $r=0.98$ ) but exhibits a systematic cold bias of  $-1.91$  K in raw retrievals. It is demonstrated that a site-specific linear bias correction reduces the MWR  $T_m$  Root Mean Square Error (RMSE) from 2.32 K to 1.43 K, significantly outperforming the empirical model. Sensitivity analysis confirms that thermodynamic uncertainty dominates the error budget, outweighing uncertainties in refractivity constants by an order of magnitude. Consequently, standard climatological retrievals diverge from the synergistic MWR-GNSS method during extreme hygrometric events, introducing systematic PWV biases exceeding 1.0 mm when moisture levels surpass 45 mm. The synergistic coupling of real-time radiometric  $T_m$  with GNSS data is therefore meaningful for generating climate-quality PWV records in semi-arid coastal regions.

## 1 Introduction

Atmospheric water vapour (WV) is the primary greenhouse gas, contributing approximately 60 % to the natural greenhouse effect and playing a vital role in regulating the Earth's thermodynamic budget (Kiehl and Trenberth, 1997; Trenberth et al., 2005). Furthermore, WV is the main driver of latent heat transport, influencing convective systems and global precipitation patterns. High-frequency variations in Precipitable Water Vapour (PWV) correlate strongly with atmospheric instability and are a key factor in the initiation of severe weather. Specifically, rapid temporal gradients in PWV often precede heavy rainfall

32 and flash floods, acting as a reliable precursor for convective storms (Brenot et al., 2013). Consequently, assimilating high-  
33 resolution PWV data into Numerical Weather Prediction (NWP) models significantly improves short-range precipitation "now-  
34 casting" (Bennitt and Jupp, 2012). Accurate PWV retrieval is especially crucial for the Eastern Mediterranean, a climate change  
35 "hotspot" warming faster than the global average (Giorgi, 2006; Lelieveld et al., 2012). This region is characterized by complex  
36 topography and land-sea contrasts, which create sharp atmospheric refractivity gradients. The Eastern Mediterranean faces a  
37 hydro-climatic paradox: a long-term drying trend ( $-0.5$  mm/decade) alongside increasing high-intensity, short-duration flash  
38 flood events (Zittis et al., 2019; Ziv et al., 2021). GNSS-derived PWV in this region exhibits strong diurnal cycles with  
39 amplitudes up to 5 mm, which are closely correlated with atmospheric instability (Ziskin Ziv et al., 2020). Despite this  
40 vulnerability, the Eastern Mediterranean currently lacks dense, continuous atmospheric profiling networks. Traditional  
41 observation methods, such as radiosondes (RS), fail to resolve these mesoscale events due to low temporal resolution (typically  
42 12-hour intervals) and significant spatial gaps (Soden and Lanzante, 1996). While satellite-based passive remote sensing offers  
43 global coverage, it is often limited by revisit times, daylight dependence, or data degradation in coastal zones due to land  
44 contamination in the microwave footprint (Bennartz and Bauer, 2003).

45 These limitations underscore the necessity for ground-based remote sensing techniques that offer continuous, all-weather  
46 operability. Ground-based Global Navigation Satellite Systems (GNSS) meteorology has emerged as a robust technique for  
47 atmospheric sounding since the seminal proposal by Bevis et al. (1992). By estimating the Zenith Total Delay (ZTD) of GNSS  
48 signals traversing the neutral atmosphere, the Zenith Wet Delay (ZWD) can be isolated by subtracting the Zenith Hydrostatic  
49 Delay (ZHD), which is accurately modeled from surface pressure observations (Saastamoinen, 1972). GNSS-derived PWV  
50 offers significant advantages, including high temporal resolution (sub-hourly), all-weather availability, and cost-efficiency by  
51 leveraging existing geodetic infrastructure (Guerova et al., 2016; Jones et al., 2020).

52 The retrieval of PWV from GNSS ZWD relies on a dimensionless conversion factor,  $\Pi$ , which is a function of the  
53 atmospheric weighted mean temperature,  $T_m$ . Defined physically as  $\int(e/T)dz/\int(e/T^2)dz$  (Askne and Nordius, 1987),  $T_m$   
54 encapsulates the thermal state of the atmospheric column. ~~Because the conversion factor~~The conversion factor ( $\Pi$ ) is nearly  
55 linearly proportional to  ~~$T_m$ , any relative error in the a 1 K error in  $T_m$  estimation strictly~~  
56 propagates as an equivalent relative error in the final PWV retrieval. ~~(assuming standard atmospheric temperatures near 280~~  
57 ~~K) introduces a relative error of approximately 0.36 % in the final IWV.~~ During severe moisture events with an PWV of  
58  $50 \text{ kg m}^{-2} \text{ mm}$ , this translates to an absolute error of  $\sim 0.18 \text{ kg mmm}^{-2}$ . Consequently, a 1 % relative error in  $T_m$  translates  
59 strictly to a 1 % relative error in PWV. Therefore, alongside the substantial errors inherent in ZTD estimation—such as  
60 mapping function inaccuracies and surface pressure interpolation for the ZHD (Ning et al., 2016)—the determination of  $T_m$   
61 remains one of the primary sources of uncertainty in GNSS meteorology. In the absence of in-situ profiles,  $T_m$  is commonly  
62 estimated using empirical regression models or global climatological models. However, earlier studies have demonstrated that  
63 empirical  $T_m$  regressions, such as the Bevis model (Bevis et al., 1992), introduce relative PWV errors of 1–2 % due to weak  $T_s$

64  $-T_m$  correlations in coastal and equatorial regions, where annual/semiannual variations are not adequately captured (Yao et  
65 al., 2014; Lan et al., 2016). Similarly, global grid-based  $T_m$  models like GPT2w achieve RMSE <4 K at ~80 % of mid-latitude  
66 sites but degrade in data-sparse areas like the Middle East and Africa, where reanalysis quality is limited (Böhm et al., 2015;  
67 Jiang et al., 2019). The Hourly Global Pressure and Temperature 2 (HGPT2) model represents a major advancement by  
68 providing hourly estimates derived from ERA5 reanalysis (Mateus et al., 2021). Despite recent validation of GPT2w and  
69 ECMWF models for Integrated-Precipitable Water Vapour (PWV) retrieval in the Mediterranean (Oikonomou et al. 2018), a  
70 critical gap exists: the quantification of vertical interpolation errors in these models, especially over complex coastal terrains.  
71 For instance, while recent validation studies in Cyprus demonstrate strong GNSS-PWV correlations (>0.6) with ERA5 during  
72 extreme precipitation, persistent reanalysis interpolation errors are highlighted in mountainous areas (Giannadaki et al., 2025).  
73 This lack of validation for HGPT2's performance in the complex topography of the Eastern Mediterranean potentially  
74 exacerbates PWV biases during extreme events.

75 An alternative approach to deriving  $T_m$  is the use of ground-based Microwave Radiometers (MWR). MWRs measure  
76 brightness temperatures at multiple frequencies to retrieve continuous vertical profiles of temperature and humidity. Ground-  
77 based MWRs have been shown to retrieve  $T_m$  with RMSE ~1–2 K in mid-latitudes, outperforming empirical models during  
78 synoptic anomalies (Cimini et al., 2010; Crewell and Löhnert, 2007; Löhnert et al., 2012). While multi-site intercomparisons  
79 reveal that MWR retrievals can exhibit upper-tropospheric cold biases (up to 5 K at >2 km altitude) (Van Malderen et al.,  
80 2014; Steinke et al., 2015), simple linear corrections can reduce RMSE by 20–40 % (Ning and Elgered, 2021). Operational  
81 GNSS–MWR synergies for  $T_m$  bias correction have documented gains in PWV accuracy (10–30 % RMSE reduction) in  
82 European networks (Vaquero-Martínez et al., 2018; Li et al., 2020). However, such applications are rare in the semi-arid  
83 Eastern Mediterranean, where MWR could critically mitigate reanalysis uncertainties.

84 This study leverages the infrastructure of the CYGMEN (Cyprus GNSS Meteorology Enhancement) project, which is  
85 establishing a dense, multi-sensor meteorological network in Cyprus. The network, termed CyMETEO, integrates a dense  
86 array of continuous GNSS stations distributed across the island. Due to the high cost and operational complexity of radiometric  
87 profiling, the network currently features a single, centralized thermodynamic 'supersite' at the Athalassa observatory, where a  
88 GNSS receiver is strictly co-located with a MWR and a RS launch facility. This unique instrumental setup provides an ideal  
89 testbed for inter-comparing atmospheric retrieval techniques in a coastal, semi-arid environment. The primary objective of this  
90 manuscript is to evaluate the accuracy of GNSS-derived PWV over the Eastern Mediterranean by assessing the performance  
91 of different  $T_m$  determination strategies. We specifically investigate the efficacy of the HGPT2 model compared to MWR-  
92 derived  $T_m$  and RS benchmarks. The study aims to quantify the error budget of GNSS-PWV and determine whether the  
93 inclusion of MWR data provides statistically significant improvements over the state-of-the-art HGPT2 model. The manuscript  
94 is organized as follows: Section 2 describes the study area and the instrumentation of the CyMETEO network; Section 3 details  
95 the methodology for GNSS processing, ZTD estimation, and the mathematical derivation of  $T_m$  from different sources; Section  
96 4 presents the validation results and statistical analysis against RS reference data; and Section 5 concludes with

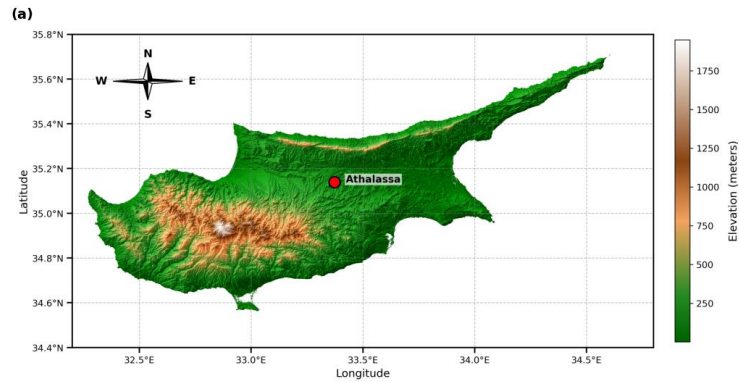
97 recommendations for operational PWV monitoring strategies in the region.

98

## 99 2 Data and Methodology

### 100 2.1 Observational Site and CYGMEN Infrastructure

101 The observational campaign was conducted at the Athalassa atmospheric observatory in Nicosia, Cyprus (35.15°N, 33.40°E,  
102 160 m a.s.l.), situated in the central Mesaoria plain. The site is characterized by complex topography, bounded by the Troodos  
103 Mountain to the southwest and the Pentadaktylos Mountain to the north, as shown in Fig. 1a. This study presents the first  
104 comprehensive analysis of radiometric data acquired under the CYGMEN infrastructure project, established to monitor the  
105 thermodynamic state of the Eastern Mediterranean atmosphere. To ensure robust thermodynamic profiling and validation,  
106 three primary datasets were collated, as shown in Table 1:



107

108

109

**Figure 1.** Location and instrumentation at Athalassa, Cyprus. (a) Site location on the island's elevation map. (b) GNSS reference station. (c) RPG-HATPRO radiometer. (d) Radiosonde balloon launching.

110

111 **Table 1:** Summary of Instrumentation and Datasets

Parameter	Microwave Radiometer (MWR)	Radiosonde (RS)	GNSS Station
-----------	----------------------------	-----------------	--------------

<b>Instrument Model</b>	HATPRO-Gen5 (RPG)	Vaisala RS41-SGP	GNSS Receiver LEICA GR50 (Collocated)
<b>Role in Study</b>	Synergistic thermodynamic profiling (temperature and humidity) and $P_{\text{WV}}$ estimation	<i>In-situ</i> "Ground Truth" Reference	ZTD Source for PWV Retrieval
<b>Observation Type</b>	Passive remote sensing (22–58 GHz)	<i>In-situ</i> vertical profile (balloon-borne)	Continuous satellite signal delay
<b>Key Variables</b>	Brightness Temp ( $T_B$ ), $T(z)$ , $\rho_v(z)$ , $P_{\text{WV}}$	$P(z)$ , $T(z)$ , $RH(z)$ , Geopotential Height	Zenith Total Delay (ZTD)
<b>Vertical Range</b>	Surface to 10 km (94 levels)	Surface to burst altitude (~30 km)	Column-integrated (single value)
<b>Temporal Resolution</b>	High frequency (~1 s raw, resampled to 15 min)	Periodic (launch dependent)	Continuous (high rate)
<b>Accuracy / Noise</b>	$T_B$ noise < 0.11 K (K-band), < 0.32 K (V-band)	$T$ : 0.3 K, $RH$ : 4 % (Manufacturer spec)	ZTD precision ~mm level
<b>Auxiliary Data</b>	Vaisala WXT536 (Rain, Surface Met)	GPS position/height	Surface Pressure

112

## 113 2.2 Instrumentation and Data Processing

### 114 2.2.1 Microwave Radiometry (MWR)

115 The RPG-HATPRO radiometer observes downwelling atmospheric brightness temperatures ( $T_B$ ) across 14 channels: seven in  
116 the K-band (22–31 GHz) sensitive to water vapour, and seven in the V-band (51–58 GHz) sensitive to oxygen for temperature  
117 profiling. This instrument enables the continuous retrieval of temperature ( $T$ ) and absolute humidity ( $\rho_v$ ) profiles on a  
118 standardized grid of 94 vertical levels from the surface up to 10 km. The vertical resolution is optimized for the planetary  
119 boundary layer (PBL), ranging from 10–30 m up to 500 m, and decreasing to 100–500 m in the free troposphere. For this  
120 study, high-frequency MWR observations were resampled to 15-minute intervals to align with GNSS processing epochs. It is  
121 a well-documented limitation of passive microwave radiometry that retrieval accuracy degrades significantly during  
122 precipitation, as liquid water on the instrument's radome heavily contaminates the measured brightness temperatures (Foth et  
123 al., 2024; Parde et al., 2025; Pakkattil et al., 2025; Ware et al., 2004). Because this study focused on the warm, dry season in  
124 the Eastern Mediterranean (March–October 2025), rainfall events were naturally sparse. Nevertheless, to ensure data integrity,  
125 real-time precipitation flags generated by the co-located Vaisala WXT536 surface weather transmitter were utilized as a strict  
126 quality-control filter. Any MWR profiles retrieved during active precipitation events were excluded from the dataset to prevent  
127 wet-radome anomalies from artificially skewing the thermodynamic bias analysis. To diagnose potential biases in the MWR-

128 derived  $T_m$ , the dataset was split into a training Set (April–June 2025) for regression modeling and a validation Set (July–  
 129 October 2025) for independent testing. In addition to thermodynamic profiling, the MWR's native retrieval algorithm possesses  
 130 the capacity to directly estimate  $\text{PWV}$  from its K-band brightness temperatures.

131 Any MWR profiles retrieved during active precipitation events were excluded from the dataset to prevent wet-radome  
 132 anomalies from artificially skewing the thermodynamic bias analysis. To mitigate  $T_m$  errors in MWR, a supervised linear  
 133 regression model was developed to calibrate the MWR observations. For robust independent validation, the collocated dataset  
 134 was separated into two distinct temporal subsets: the training Set (April – June 2025), which was used to derive the regression  
 135 coefficients, and the validation Set (July – October 2025), which was used exclusively to test the correction's performance on  
 136 unseen data. A simple linear correction model was fitted to the training data using Ordinary Least Squares (OLS) minimization.  
 137 The relationship is defined in Eq. (1) as:

$$138 \quad T_{m,corr} = \alpha \cdot T_{m,MWR} + \beta \quad (1)$$

139 where  $T_{m,corr}$  is the corrected MWR temperature,  $T_{m,MWR}$  is the raw  $T_m$  derived from the radiometer and  $\alpha$  (slope) and  $\beta$   
 140 (intercept) are the learned coefficients minimizing the residual sum of squares between the MWR and RS values. Based on  
 141 our training Set, the derived coefficients applied to the validation Set were  $\alpha = 1.0623$  and  $\beta = -15.6062$  K. In addition to  
 142 thermodynamic profiling, the MWR's native retrieval algorithm possesses the capacity to directly estimate  $\text{PWV}$  from its K-  
 143 band brightness temperatures.

144

### 145 **2.2.2 Radiosonde Data Processing**

146 To establish a rigorous validation dataset,  $\text{PWV}$  was derived from high-resolution vertical profiles obtained from collocated  
 147 radiosonde launches. A strict collocation window was applied, where MWR profiles were averaged within  $\pm 30$  minutes of the  
 148 balloon launch time. The raw telemetry data, comprising pressure ( $P$ ), temperature, and dew point temperature ( $T_d$ ), were  
 149 processed to derive the total columnar water vapour content (in  $\text{kg m}^{-2}$ ) through the vertical integration of specific humidity,  
 150 assuming the atmosphere is in hydrostatic equilibrium. The determination of the necessary moisture variables relied on the  
 151 Magnus-Tetens approximation, which provides a widely accepted empirical relationship for saturation vapour pressure. First,  
 152 the actual vapour pressure ( $e$ , in hPa) was computed directly from the dew point temperature ( $T_d$ , in  $^{\circ}\text{C}$ ). This calculation  
 153 utilized the coefficients defined by Bolton (1980), which are optimized for saturation vapour pressure over liquid water in the  
 154 meteorological temperature range, as shown in Eq. (2):

$$155 \quad e = 6.112 \cdot \exp\left(\frac{17.67 \cdot T_d}{T_d + 243.5}\right) \quad (2)$$

156 Subsequently, the specific humidity ( $q$ , in  $\text{kg kg}^{-1}$ ) was derived via Eq. (3), representing the mass mixing ratio of water vapour  
 157 to the total moist air parcel:

$$158 \quad q = \frac{\epsilon \cdot e}{P - (1 - \epsilon) \cdot e} \quad (3)$$

159 where  $P$  is the static pressure (hPa) and  $\epsilon \approx 0.622$  represents the ratio of the molecular weight of water vapour to that of dry  
160 air. Once the specific humidity profile was established, the  $\text{PWV}$  was calculated by integrating  $q$  with respect to pressure. The  
161 retrieval algorithm employed the trapezoidal rule for numerical integration, which approximates the integral as the sum of  
162 discrete atmospheric layers (Eq. 4):

$$163 \quad I_{\text{WV}} = \frac{1}{g} \sum_{i=0}^{N-1} \frac{q_i + q_{i+1}}{2} \cdot |P_{i+1} - P_i| \quad (4)$$

164 where  $g$  is the gravity dependent on altitude,  $g(\phi, h)$ , where  $\phi$  represents the Geodetic latitude and  $h$  is the orthometric height.  
165  $P$  is converted to Pascals ( $Pa$ ) prior to integration and  $N$  represents the total number of vertical levels in the RS profile. It  
166 should be noted that while the trapezoidal rule can theoretically overestimate the integral of an exponentially decaying profile,  
167 the Vaisala RS41-SGP provides high-frequency 1-second telemetry (yielding a vertical spatial resolution of approximately 5  
168 to 8 meters). At this exceptionally fine resolution, the linear approximation between measurement levels effectively converges  
169 with the true atmospheric profile, rendering any systematic integration bias mathematically negligible. Also, it should be  
170 noted that  $I_{\text{WV}}$ , representing the mass column integral in  $\text{kg m}^{-2}$ , is physically and numerically equivalent to  $\text{PWV}$  expressed  
171 as a depth in millimeters (mm), assuming the standard density of liquid water ( $1000 \text{ kg m}^{-3}$ ). A strict quality assurance protocol  
172 was implemented to ensure vertical completeness; only radiosonde flights that successfully maintained continuous telemetry  
173 up to the 10 km AGL integration ceiling were included in the final comparative dataset. While the term  $\text{PWV}$  is frequently  
174 used when discussing direct profile integration from the MWR and RS, this study uses  $\text{PWV}$  (mm) as the standardized final  
175 retrieval metric to align with operational meteorological and forecasting conventions. It is important to note that while the  
176 nominal manufacturer uncertainty for the Vaisala RS41 humidity sensor is stated as 4 % for individual profile measurements,  
177 the uncertainty of the resulting  $\text{PWV}$  is significantly lower. Because  $\text{PWV}$  is computed by integrating hundreds of discrete  
178 measurements across the vertical column (Eq. 3), uncorrelated random sensor noise is largely suppressed through statistical  
179 cancellation. Consequently, the integrated variables derived from the radiosonde, such as  $\text{PWV}$  and the  $T_m$ , possess the  
180 requisite precision to serve as a robust 'ground truth' standard for evaluating the finer relative uncertainties (1–2 %) associated  
181 with the GNSS and MWR retrievals. To ensure a rigorous and direct intercomparison with the active MWR, the radiosonde  
182 integration was strictly confined to a maximum altitude of 10 km Above Ground Level (AGL). This vertical cutoff was  
183 deliberately chosen to exactly match the 10 km ceiling of the standard RPG-HATPRO retrieval grid. While GNSS integrates  
184 delays through the entire atmosphere, bounding the in-situ reference data is mathematically necessary to isolate profiling  
185 performance. It is well established that this 10 km threshold does not introduce a systematic dry bias when comparing against  
186 total-column GNSS (Van Baelen et al., 2005). Furthermore, ambient temperatures at this altitude range from  $-40 \text{ }^\circ\text{C}$  to  $-50$   
187  $^\circ\text{C}$ , strictly limiting the saturation vapour pressure. Consequently, the residual water vapour between 10 km and the tropopause  
188 is thermodynamically constrained to fractions of a millimeter. Omitting this minute residual mass is functionally negligible,  
189 as it falls well within the overall baseline uncertainty (typically 1–2 mm) of the total-column radiosonde  $\text{PWV}$  retrieval.

190

### 191 2.2.3 GNSS Data Processing

192 ZTD estimates were derived from the collocated Leica GR50 receiver (station NICO) using the Tefnut PP software (Douša et  
193 al., 2014). The processing employed a Precise Point Positioning (PPP) strategy with an elevation cutoff angle of 10°. To  
194 account for tropospheric mapping errors, the Vienna Mapping Function 1 (VMF1) was applied. Station coordinates were  
195 constrained to the IGS14 reference frame, and satellite orbits and clock corrections were utilized from IGS Ultra-Rapid  
196 products. While IGS Final products are the gold standard for historical climate reprocessing due to their minimal orbital  
197 uncertainty, this study deliberately utilized IGS Ultra-Rapid products to evaluate the proposed synergistic retrieval architecture  
198 under near real-time operational constraints. Because a primary application of continuous GNSS-PWV is its assimilation into  
199 short-range NWP for severe weather 'nowcasting', it is crucial to assess system performance using the satellite orbits and clocks  
200 actually available during active forecasting. Although Ultra-Rapid products introduce a slight degradation in ZTD precision  
201 compared to Final products, this uncertainty (typically fractions of a millimeter in PWV) remains negligible compared to the  
202 massive, multi-millimeter systematic errors introduced by static thermodynamic modeling, which is the primary focus of this  
203 investigation. While modern Numerical Weather Prediction systems frequently assimilate ZTD directly to avoid conversion  
204 uncertainties, deriving an accurate physical PWV product remains essential. PWV serves as an intuitive, absolute moisture  
205 metric heavily utilized by operational forecasters for severe weather nowcasting, and is fundamentally necessary for building  
206 long-term, cross-instrument climatological records. To isolate the ZWD, the ZHD was precisely calculated using continuous,  
207 co-located surface pressure observations obtained directly from the Vaisala WXT536 weather transmitter installed at the site,  
208 rather than relying on interpolated pressure fields. ZTD values were estimated at 15-minute intervals, directly aligning with  
209 the temporal resolution of the MWR. It must also be noted that the computation of ZHD is significantly dependent on the  
210 assumed value of the dry refractivity constant,  $k_1$ . As established by Bevis et al. (1994) and further evaluated by Healy (2011),  
211 while  $k_1$  is known to a high degree of relative accuracy, its residual fractional uncertainty introduces a persistent systematic  
212 bias into the ZHD estimation. Because ZWD is isolated by subtracting ZHD from the total delay, this  $k_1$ -induced bias directly  
213 propagates into the final PWV error budget, acting alongside the conversion uncertainties analyzed later in this study.

### 215 2.3 Thermodynamic Modeling and Synergistic Retrieval Strategy

216 The conversion of GNSS-derived ZWD to PWV is governed by a proportionality factor,  $\Pi$ , whose accuracy is largely dictated  
217 by the  $T_m$ . To assess the fidelity of thermodynamic inputs for GNSS meteorology, we evaluated three distinct  $T_m$  derivation  
218 strategies. For profile-resolving instruments (MWR and RS),  $T_m$  values were computed by integrating the vertical profiles of  
219 physical temperature,  $T(z)$  (K), and absolute humidity,  $\rho_v(z)$  ( $\text{kg m}^{-3}$ ). Consistent with Bevis et al. (1992),  $T_m$  is defined as the  
220 mean temperature of the atmosphere weighted by the water vapour partial pressure, which can be expressed in terms of vapour  
221 density as shown in Eq. (5):

$$T_m = \frac{\int_{z_{surf}}^{z_{top}} \rho_v(z) dz}{\int_{z_{surf}}^{z_{top}} \frac{\rho_v(z)}{T(z)} dz} \quad (5)$$

In practice, the continuous integrals were discretized using the trapezoidal rule from the surface ( $z_{surf}$ ) to the highest available profile level ( $z_{top}$ ). This approach assumes linear variation of  $T$  and  $\rho_v$  between measurement levels. For standalone GNSS retrieval (where no dynamic profiles are available),  $T_m$  was derived from the HGPT2 (Hourly Global Pressure and Temperature 2) model (Mateus et al., 2021). HGPT2 is an advanced 'blind' empirical model, meaning its outputs are independent of the specific observational year. While dynamic NWP models provide superior real-time meteorological data, 'blind' models like HGPT2 remain heavily utilized in standard geodetic GNSS processing where real-time meteorological or NWP data streams are unavailable. It is constructed from a comprehensive 20-year historical baseline of atmospheric data from the ERA5 global reanalysis. Unlike standard static climatologies, HGPT2 leverages the full ERA5 spatial resolution ( $0.25^\circ \times 0.25^\circ$ ) and provides temporal resolution at 1-hour intervals for any given Day of Year (DOY). It achieves this by employing a time-segmentation concept, modeling thermodynamic variables via long-term mean values combined with annual, semi-annual, and quarterly periodic functions.

Applying the linear correction model (as formulated in Section 2.2.1) successfully re-centers the error distribution. To quantify the benefits of sensor synergy in integrated water vapour estimation, this study defines and contrasts two distinct GNSS PWV retrieval architectures. The first, "Standard Retrieval" which is a control method utilizes the  $ZTD_{GNSS}$  combined with the  $T_m$  derived empirically from the HGPT2 climatological model (Böhm et al., 2015). Second "Synergistic Retrieval" which proposed method couples  $ZTD_{GNSS}$  with a physical  $T_m$  derived directly from a collocated MWR. For the synergistic approach, the dimensionless conversion factor ( $\Pi$ ) was calculated dynamically using the MWR-derived  $T_m$  following Eq. (6) and Eq. (7).

$$PWV = \Pi \cdot ZWD \quad (6)$$

$$\Pi = \frac{10^6}{\rho_w R_v [k_2' + (k_3/T_m)]} \quad (7)$$

where  $\rho_w$  represents the density of liquid water ( $1000 \text{ kg m}^{-3}$ ) and  $R_v$  is the specific gas constant for water vapour ( $461.52 \text{ J kg}^{-1} \text{ K}^{-1}$ ). To assess the sensitivity of the  $\Pi$  to the choice of thermodynamic coefficients, three widely used formulations were employed in this study, following Davis (1985)/Thayer (1974), Bevis et al. (1994), and Rüeiger (2002), as shown in Table 2:

**Table 2.** Refractivity constants used in the sensitivity analysis of the  $\Pi$  factor, based on three commonly adopted formulations.

Method	$k_2$ (K hPa <sup>-1</sup> )	$k_3$ (K <sup>2</sup> hPa <sup>-1</sup> )	$k_2'$ (K hPa <sup>-1</sup> )
Davis (1985) / Thayer (1974)	64.79	$3.776 \times 10^5$	16.52
Bevis et al. (1994)	70.40	$3.739 \times 10^5$	22.13

Rüeger (2002)	71.295	$3.7546 \times 10^5$	22.97
---------------	--------	----------------------	-------

To rigorously quantify the uncertainty in the final ~~IPWV~~ (which is numerically equivalent to PWV) retrieval and avoid fragmented error attributions, standard error propagation must be applied to the fundamental conversion Eq. 6. Assuming the uncertainties in the wet delay and the conversion factor are uncorrelated, the variance of the final ~~PWV~~ ( $\sigma_{\text{PWV}}^2$ ) is expressed using partial derivatives as in Eq. (8):

$$\sigma_{\text{PWV}}^2 = \left( \frac{\partial \text{PWV}}{\partial \text{ZWD}} \right)^2 \sigma_{\text{ZWD}}^2 + \left( \frac{\partial \text{PWV}}{\partial \pi} \right)^2 \sigma_{\pi}^2 \quad (8)$$

Evaluating these primary partial derivatives yields the proportional contributions of the geodetic and thermodynamic components as shown in Eq. (9):

$$\sigma_{\text{PWV}}^2 = \pi^2 \sigma_{\text{ZWD}}^2 + \text{ZWD}^2 \sigma_{\pi}^2 \quad (9)$$

The uncertainty in the conversion factor ( $\sigma_{\pi}^2$ ) is itself a compound term driven by the  $T_m$  and the static atmospheric refractivity constants ( $k_2'$  and  $k_3$ ). Its variance is defined via partial derivatives as shown in Eq. (10):

$$\sigma_{\pi}^2 = \left( \frac{\partial \pi}{\partial T_m} \right)^2 \sigma_{T_m}^2 + \left( \frac{\partial \pi}{\partial k_2'} \right)^2 \sigma_{k_2'}^2 + \left( \frac{\partial \pi}{\partial k_3} \right)^2 \sigma_{k_3}^2 \quad (10)$$

The sensitivity of the conversion factor strictly to  $T_m$  (the dynamic thermodynamic variable evaluated in this study) is quantified by its partial derivative and it represented as Eq. (11):

$$\frac{\partial \pi}{\partial T_m} = \pi \left[ \frac{k_3}{T_m^2 (k_2' + \frac{k_3}{T_m})} \right] \quad (11)$$

This consolidated formulation establishes the exact mathematical limits of thermodynamic error propagation. As demonstrated in the sensitivity analysis (Section 3.4), this framework accurately isolates the dynamic uncertainties driven by  $T_m$  from the baseline static biases introduced by the chosen refractivity constants.

## 2.4 Diagnostic Parameters and Error Analysis

The vertical structure of the atmosphere was analyzed by segregating the dataset into two regimes: the PBL (0-2 km), where water vapour is concentrated, and the Free Troposphere (> 2 km). Additionally, the water vapour scale height ( $H_v$ ) was calculated to parameterize the vertical distribution of moisture.  $H_v$  was derived for both RS and MWR by fitting an exponential decay function (Eq. 12) to the absolute humidity profile ( $\rho_v$ ).

$$\rho_v(z) = \rho_{v,0} \cdot \exp\left(-\frac{z}{H_v}\right) \quad (12)$$

where  $\rho_v(z)$  is the absolute humidity at height  $z$ , and  $\rho_{v,0}$  is the surface humidity. This curve fitting was deliberately restricted to the lowest 4 km of the atmosphere. Because this layer contains the vast majority (>90%) of the tropospheric water vapour mass, bounding the fit prevents the algorithm from heavily weighting near-zero, noisy upper-tropospheric values that mathematically degrade the fit for the boundary layer. Furthermore, the scale height metric fundamentally assumes the

276 atmosphere conforms to a well-behaved exponential decay. Profiles yielding  $H_v$  values outside the physically realistic range  
 277 of 0.1 to 4.0 km were excluded from the statistical analysis to prevent artificial statistical skewing during complex  
 278 meteorological states (e.g., deep convective mixing) where the underlying exponential model is invalid. Forcing a  
 279 mathematical fit onto these non-exponential profiles yields physically meaningless artifacts. Therefore, a Quality Assurance  
 280 filter was applied, bounding the analysis to the physically realistic range of  $0.1 \text{ km} < H_v < 4.0 \text{ km}$ . Profiles yielding values  
 281 outside this range were discarded because they indicate the underlying exponential model itself is invalid for that specific  
 282 atmospheric profile, preventing artificial statistical skewing in the instrument intercomparison. Profiles yielding  $H_v$  values  
 283 outside the physically realistic range of 0.1 to 4.0 km were excluded from the statistical analysis. To evaluate the performance  
 284 limitations of standard climatological models under varying hygrometric conditions, the systematic error ( $\Delta PWV$ ) was defined  
 285 as the residual between the synergistic and standard approaches (Eq. 13):

$$286 \quad \Delta PWV = PWV_{\text{Synergistic}} - PWV_{\text{Standard}} \quad (13)$$

287 The dataset was stratified into discrete bins of 5 mm PWV to isolate regimes of moisture abundance. Within each bin, the  
 288 mean bias and  $\pm 1\sigma$  uncertainty were computed. These statistics were utilized to determine the "Systematic Bias Threshold,"  
 289 defined herein as the specific hygrometric threshold where the systematic model error exceeds 1 mm. Finally, the propagation  
 290 of thermodynamic uncertainty into the moisture retrieval was quantified via linear regression analysis. This compared the  
 291 relative error in  $T_m$  (HGPT2 vs. MWR) against the resulting relative error in PWV, serving as an empirical verification of the  
 292 theoretical sensitivity approximation given in Eq. (14):

$$293 \quad \frac{\Delta PWV}{PWV} \approx \frac{\Delta T_m}{T_m} \quad (14)$$

## 294 **3 Results**

295 The following evaluation follows a top-down diagnostic approach. First, the macroscopic baseline performance of the final  
 296 derived moisture products is established. Subsequently, the underlying thermodynamic variables driving these discrepancies  
 297 are isolated, culminating in the development of a targeted calibration scheme to mitigate the identified biases.

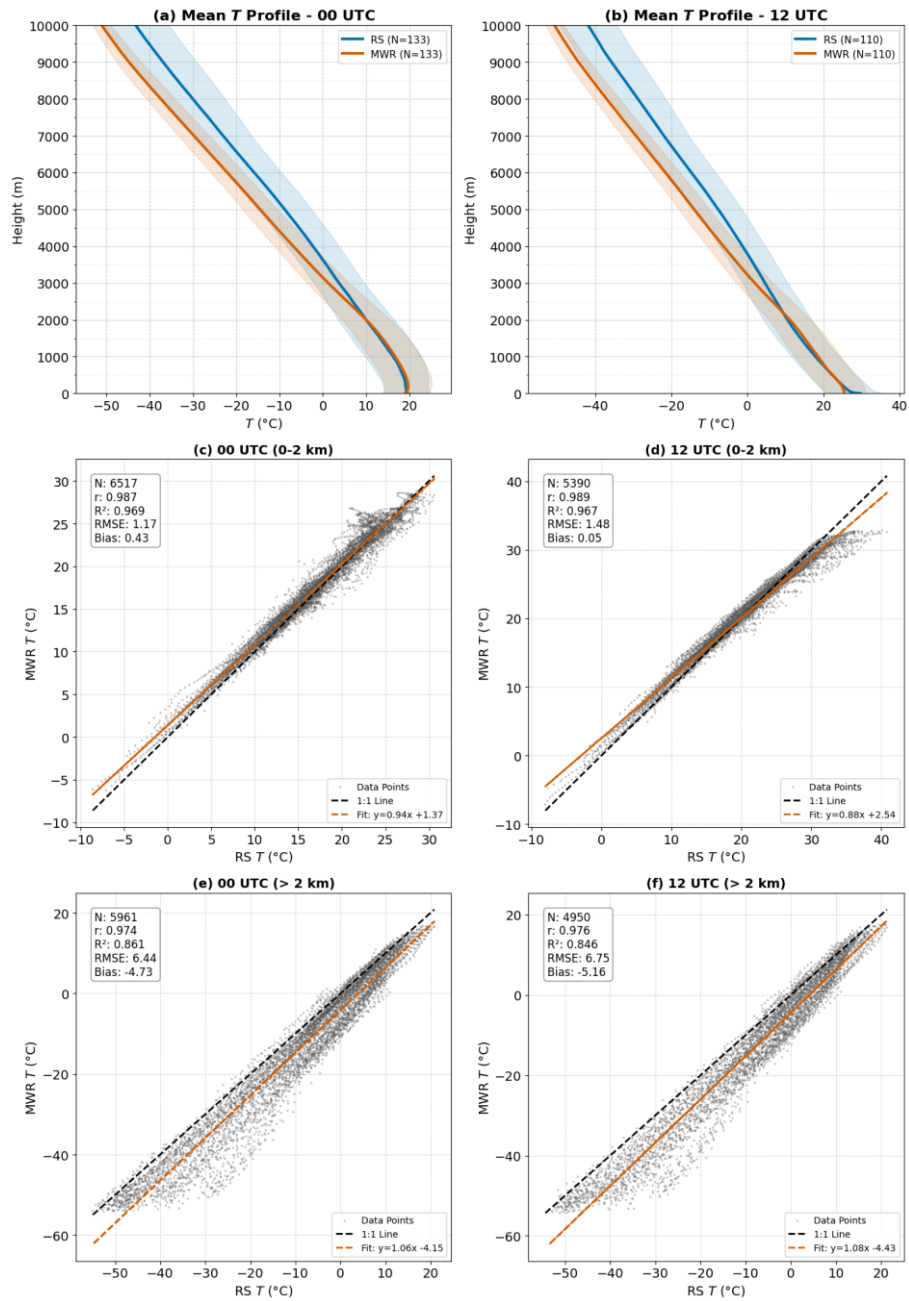
### 299 **3.1 Temperature and Humidity Profile Validation**

300 MWR-retrieved temperature  $T$  and  $\rho_v$  profiles were validated against collocated RS observations at 00:00 UTC and 12:00 UTC  
 301 during March–October 2025. Profiles were stratified into the planetary boundary layer (PBL; 0–2 km) and free troposphere  
 302 (>2 km), as shown in Figs. 2 and 3. Mean vertical temperature profiles show agreement between MWR and RS (Fig. 2a–b).  
 303 In the boundary layer (0–2 km), MWR retrieves temperature with high precision ( $r > 0.98$ ,  $RMSE < 1.5 \text{ K}$ ). Above 2 km, a cold  
 304 bias is observed in the MWR retrieval, reaching  $-5.16 \text{ K}$  at 12 UTC (Fig. 2f). Despite this bias, the linearity remains strong  
 305 ( $r \approx 0.97$ ), indicating the sensor captures relative thermal variations aloft despite the absolute offset. This confirms the trend

306 observed in the mean profiles, where the MWR underestimates temperatures in the mid-to-upper troposphere. Furthermore,  
307 horizontal balloon drift driven by prevailing winds inevitably causes the radiosonde to sample a different atmospheric volume  
308 than the MWR's strict zenith view. While this spatiotemporal mismatch introduces random scatter into the upper-level  
309 comparisons, it does not artificially skew the systematic biases identified in this study. Consequently, the RMSE increases  
310 substantially to approximately 6.4–6.7 °C. The stark contrast in accuracy between the lower and upper troposphere is a known  
311 characteristic of ground-based microwave radiometry (Parde et al., 2025; Pakkattil et al., 2025). The high accuracy below 2  
312 km is attributed to the high information content of the opaque V-band channels (51–58 GHz), whose weighting functions peak  
313 near the surface. Above 2 km, these weighting functions broaden significantly, reducing vertical resolution and causing a  
314 "smearing" effect where the instrument provides a volume-averaged temperature rather than a precise point measurement. The  
315 observed cold bias is likely a result of the retrieval algorithm (e.g., neural network) relying heavily on a climatological *a priori*  
316 dataset that does not perfectly represent the thermal conditions of the transition season observed, or systematic offsets in the  
317 radiative transfer model (absorption coefficients) used for training.

318 The mean  $\rho_v$  profiles (Figs. 3a–b) show the expected exponential decrease of moisture with height. At 00 UTC, the profiles  
319 align reasonably well. However, at 12 UTC, the MWR profile exhibits a structural deviation between 1–2 km, failing to capture  
320 the smooth moisture gradient recorded by the RS. This discrepancy may be attributed to the MWR's limited vertical resolution  
321 during periods of active daytime mixing or complex humidity layering. The retrieval of humidity in the lower atmosphere  
322 shows moderate agreement but is less accurate than the temperature retrievals. Performance is notably better at night (00 UTC)  
323 with  $r$  of 0.878 and RMSE of 1.98 g m<sup>-3</sup>. At 12 UTC, the correlation drops to 0.744, and the scatter increases (RMSE = 2.31 g  
324 m<sup>-3</sup>). Because the integrated mass of the water vapour column is physically and numerically equivalent to its depth (assuming  
325 the standard density of liquid water), this physical quantity is exclusively referred to as PWV expressed in millimeters (mm)  
326 throughout this study to align with operational meteorological conventions. A negative bias persists at both times (–0.51 g m<sup>-3</sup>  
327 at 00 UTC and –0.91 g m<sup>-3</sup> at 12 UTC), indicating a tendency for the MWR to underestimate moisture content in the boundary  
328 layer, particularly during the day. Surprisingly, the statistical linearity for  $\rho_v$  improves slightly or remains stable above 2 km,  
329 likely due to the lower overall magnitude of humidity at these heights. The correlation coefficients remain stable (~0.87). In  
330 contrast to the lower levels, the bias shifts to slightly positive values (0.23 g m<sup>-3</sup> at 00 UTC and 0.46 g m<sup>-3</sup> at 12 UTC),  
331 suggesting a slight moist bias in the MWR retrievals aloft. The linear fits (Figs. 3e–f) align closely with the 1:1 line, with  
332 slopes near unity (0.90 and 1.00), indicating that the MWR effectively captures the free tropospheric humidity trends despite  
333 the lower absolute values. The difficulty in retrieving accurate  $\rho_v$  profiles, particularly at 12 UTC, stems from the limited  
334 vertical resolution of the K-band channels (22–31 GHz). Unlike temperature profiling, humidity profiling offers very few  
335 independent degrees of freedom (typically <3), making it difficult for the MWR to resolve sharp vertical gradients often present  
336 at the top of the convective boundary layer during the daytime. The structural deviation and underestimation are common  
337 issues linked to the "smoothing" error inherent in passive radiometry, where sharp moisture inversions are averaged out.

338 Furthermore, the persistent bias suggests potential uncertainties in the water vapour absorption models (spectroscopic  
 339 parameters) or non-representative training data used in the retrieval algorithm.  
 340



341  
 342 **Figure 2.** Comparison of radiosonde and microwave radiometer (MWR) temperature profiles: (a–b) Mean vertical temperature (T) profiles  
 343 at 00 and 12 UTC with variability shading; (c–f) Scatter comparisons for the lower (0–2 km) and upper (>2 km) atmosphere at both times.  
 344

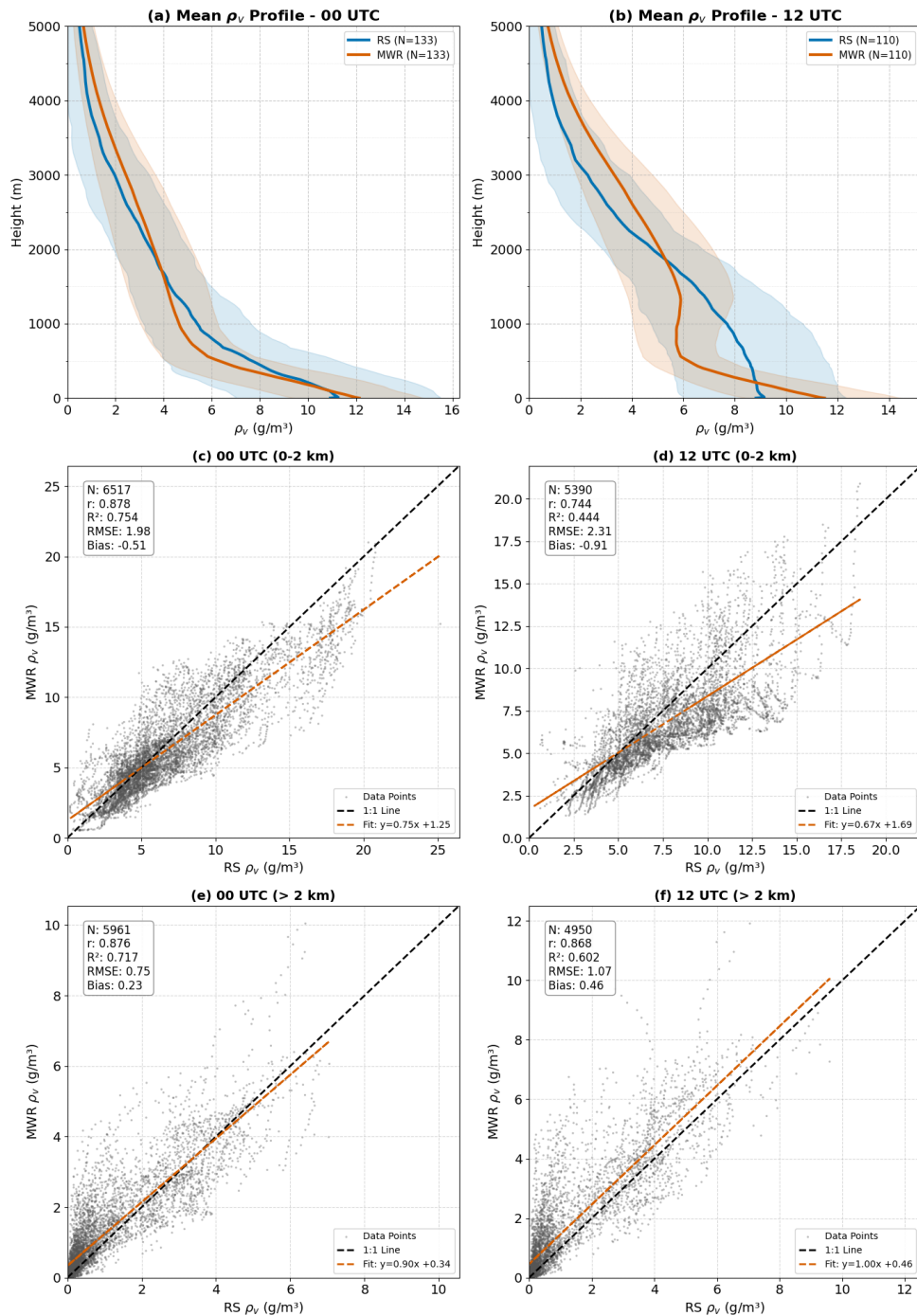


**Figure 3.** Comparison of radiosonde and microwave radiometer (MWR) absolute humidity ( $\rho_v$ ) profiles: (a–b) Mean vertical  $\rho_v$  profiles at 00 and 12 UTC with variability shading; (c–f) Scatter comparisons for the lower (0–2 km) and upper (>2 km) atmosphere at both times.

### 3.2 Integrated-Precipitable Water Vapour (PIWV) and Scale Height ( $H_v$ ) Validation

350 Unlike vertical profiling, the MWR excels in measuring total column quantities. The comparison with RS yields an excellent  
351 correlation ( $r=0.971$ ) and a low RMSE of  $1.72 \text{ kg m}^{-2}$ . This performance disparity—superior P~~F~~WV versus degraded profiles—  
352 confirms that while the sensor cannot resolve vertical structural details due to smoothing error, the radiometric brightness  
353 temperature in the K-band remains strictly proportional to the total precipitable water mass. The GNSS-derived P~~F~~WV shows  
354 a slight negative bias relative to RS ( $-0.45 \text{ kg m}^{-2}$ ), whereas it relative to the MWR exhibits a positive bias ( $+0.45 \text{ kg m}^{-2}$ ). The  
355 cumulative offset observed in the MWR-GNSS intercomparison ( $+0.89 \text{ kg m}^{-2}$ ) highlights the systematic differences in  
356 calibration and retrieval assumptions between active (GNSS) and passive (MWR) techniques. The GNSS underestimation is  
357 likely driven by errors in the  $T_m$  derived from the static HGPT2 model, a hypothesis further explored in Section 3.4. To further  
358 diagnose the structural limitations of the retrievals, we evaluated the water vapour  $H_v$ . While  $H_v$  is admittedly a single-  
359 parameter representation of the complex atmospheric moisture profile, it is a crucial parameter that provides a representative  
360 value for the rate at which water vapour decreases with altitude—a key factor in understanding atmospheric stability, cloud  
361 formation, and radiative transfer processes. In this study, it is utilized specifically as a diagnostic metric to quantify the vertical  
362 structural limitations of passive microwave remote sensing. The comparison of  $H_v$  calculated from RS and MWR profiles is  
363 shown in Fig. 5. Unlike the high-fidelity P~~F~~WV retrievals, the MWR-derived scale height shows negligible correlation with  
364 RS observations ( $r=0.25$ ,  $R^2=-2.87$ ) and a massive systematic positive bias of  $0.62 \text{ km}$ . The histograms (Fig. 5b) further  
365 elucidate this discrepancy: while the RS scale heights follow a narrow, physically realistic distribution centered around a mean  
366 ( $\mu$ ) of  $1.51 \text{ km}$ , the MWR distribution is artificially broad and shifted to significantly higher values ( $\mu=2.13 \text{ km}$ ).

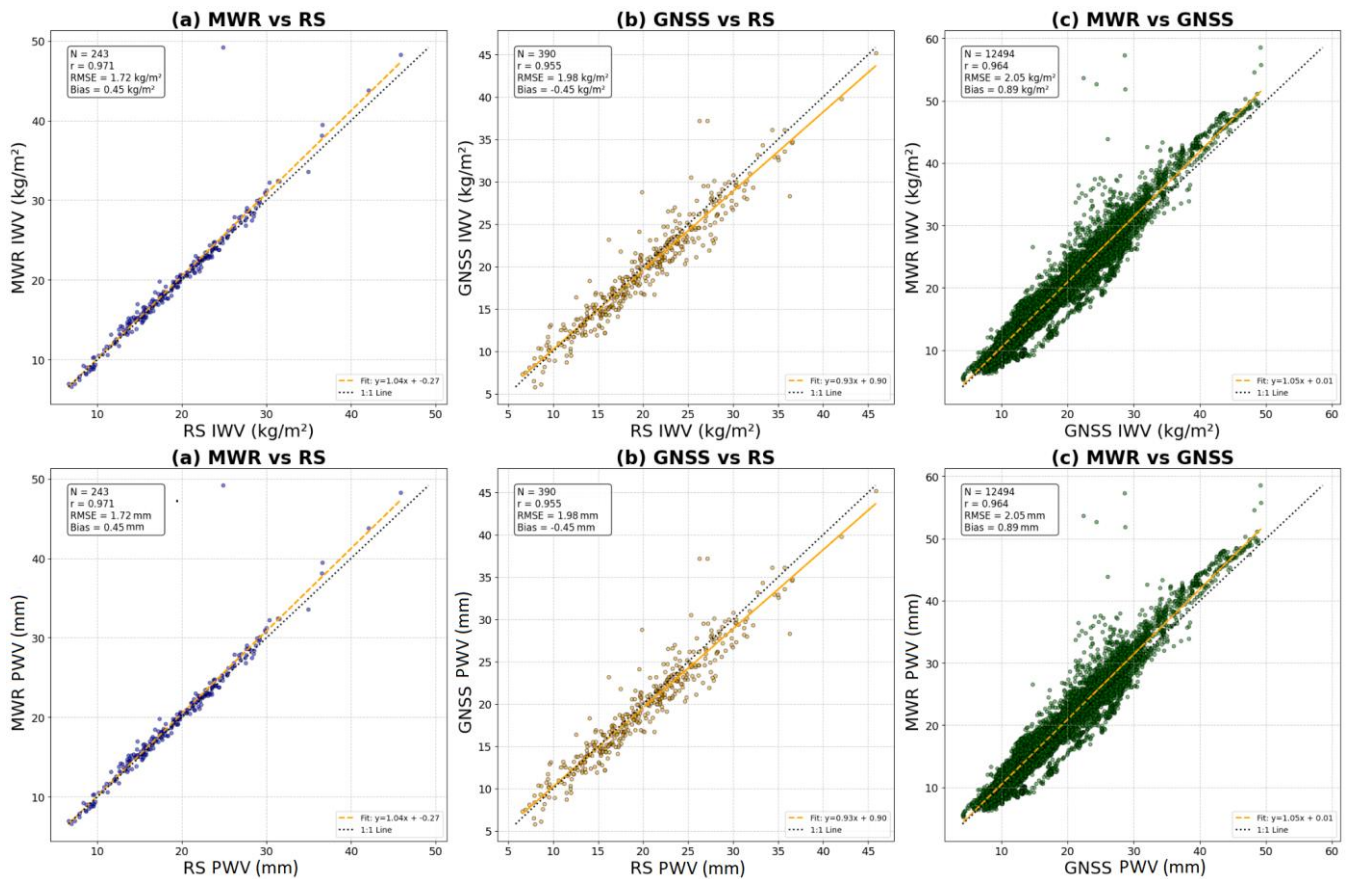
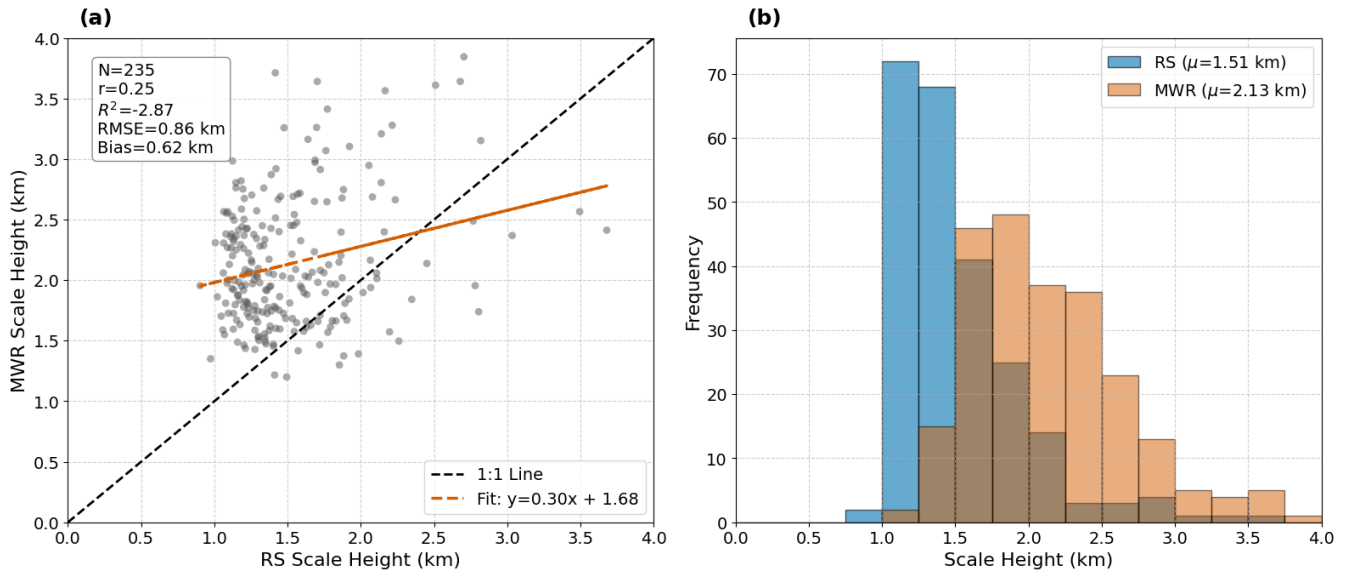


**Figure 4.** Intercomparison of integrated-precipitable water vapour ( $P_{I}WV$ ) retrieved from Microwave Radiometer (MWR), GNSS, and Radiosonde observations. (a) MWR  $P_{I}WV$  versus radiosonde  $P_{I}WV$ , (b) GNSS  $P_{I}WV$  (derived using HGPT2  $T_m$ ) versus radiosonde  $P_{I}WV$ , and (c) MWR  $P_{I}WV$  versus GNSS  $P_{I}WV$  (derived using HGPT2  $T_m$ ).

The large scatter and ambiguity in the MWR estimates—which completely dwarf the individual least-squares fit uncertainties of the exponential regression—are a direct consequence of the instrument's physical limitations.  $H_v$  is highly sensitive to the sharp vertical gradient of humidity at the top of the planetary boundary layer. However, the K-band channels (22–31 GHz) utilized for humidity profiling possess broad weighting functions, restricting the vertical degrees of freedom to typically fewer than three. Because the MWR lacks the vertical resolution to capture sharp moisture inversions, the retrieval algorithm mathematically smears the moisture mass upward. This inherent 'smoothing error' artificially elongates the vertical moisture profile, effectively inflating the calculated e-folding depth. Therefore, the inclusion of this  $H_v$  analysis serves to transparently demonstrate a critical operational boundary: while the MWR is an excellent standard for  $P_{I}WV$ , it is significantly unreliable and mathematically unsuited for characterizing vertical moisture compactness. The significant deviations observed in these macroscopic retrieval products necessitate a deeper investigation into the intermediate thermodynamic variables driving the conversion process. Consequently, the isolated performance of the  $T_m$  is evaluated in Section 3.3, followed by the introduction of a post-retrieval MWR calibration scheme in Section 3.4 designed to mitigate these native biases.

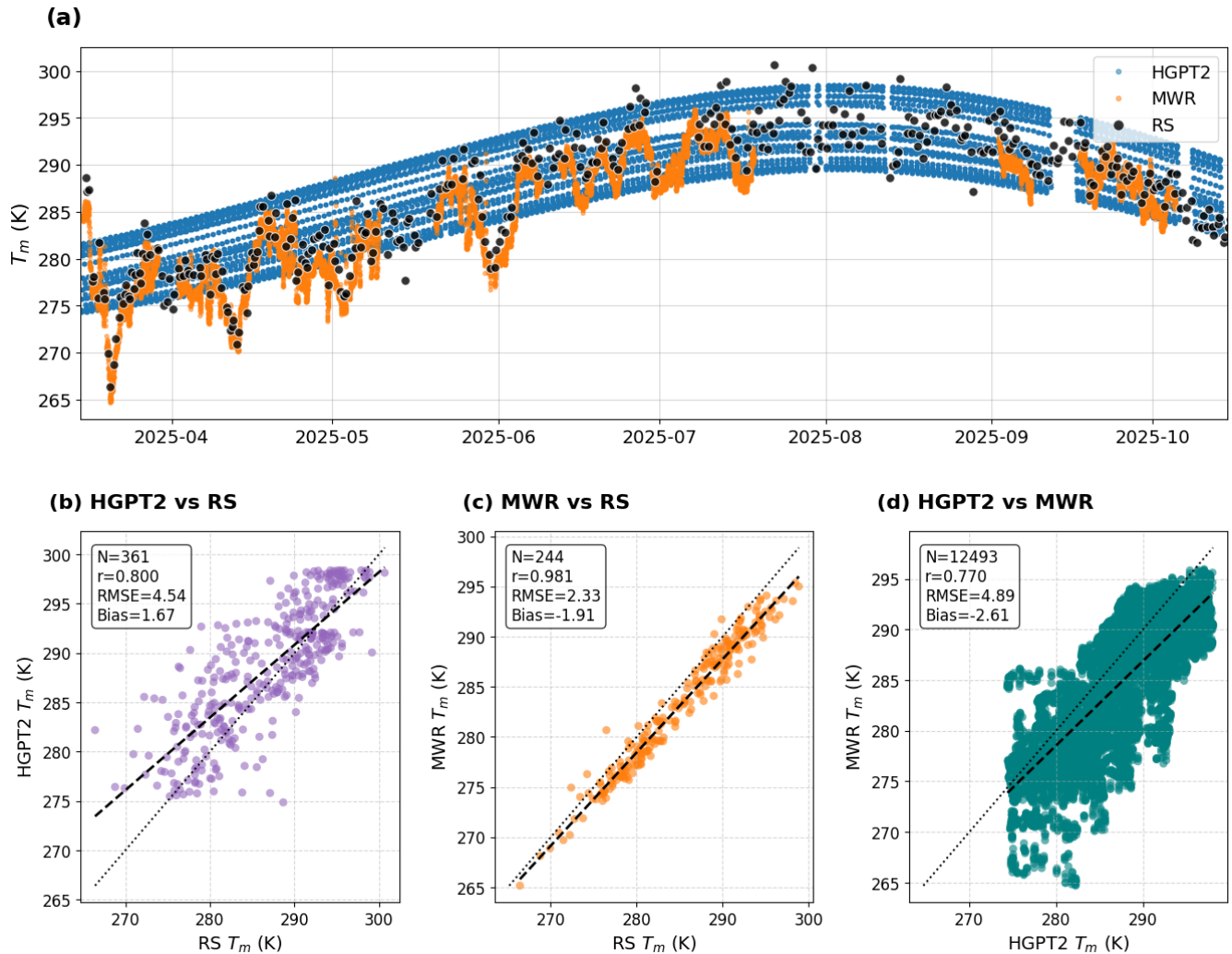


384  
385 **Figure 5:** Comparison of scale height from radiosonde (RS) and microwave radiometer (MWR): (a) Scatter plot with 1:1 line and linear fit,  
386 including summary statistics; (b) Frequency distributions showing mean scale heights for RS and MWR.  
387

### 388 3.3 Weighted Mean Temperature ( $T_m$ ) Validation

389 The accurate estimation of the  $T_m$  is critical for converting GNSS-derived ZWD into PWV. The performance of  $T_m$  derived  
390 from the MWR and the empirical GPT2w model (HGPT2) was evaluated against RS measurements, which serve as the "ground  
391 truth." The results are presented in Fig. 6. The time series (Fig. 6a) illustrates the seasonal evolution of  $T_m$  from April to October  
392 2025. The Radiosonde observations (black dots) show significant variability, capturing synoptic-scale weather fluctuations.  
393 The MWR-derived  $T_m$  (orange dots) tracks these fluctuations with remarkable precision, overlaying the RS points almost  
394 perfectly. In stark contrast, the HGPT2 model (blue dots) provides a smooth, climatological curve. While it captures the general  
395 seasonal trend, it completely misses the day-to-day thermodynamic variability, often overestimating  $T_m$  during cooler transient  
396 events and underestimating it during warmer anomalies. The empirical model shows only moderate performance ( $r=0.800$ )  
397 with a substantial spread ( $RMSE = 4.54$  K). A systematic positive bias of 1.67 K indicates that HGPT2 generally overestimates  
398 the atmospheric temperature profile in this region. The scatter plot reveals a diffuse, "cloud-like" distribution, confirming its  
399 inability to capture real-time atmospheric dynamics. The MWR demonstrates superior performance, achieving a near-perfect  
400 correlation ( $r=0.981$ ). The RMSE is significantly reduced to 2.33 K, which is nearly half the error of the empirical model.  
401 Interestingly, the MWR exhibits a negative bias of  $-1.91$  K, suggesting a systematic underestimation of  $T_m$ . Crucially, this bias  
402 does not originate in the free troposphere, but rather in the planetary boundary layer (0–3 km). Since  $T_m$  is weighted by water  
403 vapour pressure, this "cold bias" indicates the MWR is underestimating the intense near-surface heating or the sharp lapse  
404 rates characteristic of the Nicosia environment. Despite this offset, the tight linearity indicates that MWR is an excellent source  
405 for capturing real-time  $T_m$  variations. Comparing the large dataset of MWR against HGPT2 ( $N=12,493$ ) confirms the

406 discrepancy between dynamic and static modeling. The correlation is lower ( $r=0.770$ ) and the scatter is large (RMSE = 4.89  
 407 K), further proving that static empirical models are insufficient for high-precision GNSS meteorology compared to dynamic  
 408 radiometer measurements. While errors in ZTD estimation contribute significantly to the overall uncertainty budget, the  
 409 specific error introduced during the conversion from delay to water vapour is linearly dependent on the accuracy of  $T_m$ .  
 410 Assuming a given ZTD, a standard rule of thumb states that a 1 % relative error in  $T_m$  translates to roughly a 1 % relative error  
 411 in the resulting PWV. By switching from a static model (HGPT2,  $\sim 4.5$  K error) to a dynamic sensor (MWR,  $\sim 2.3$  K error),  
 412 the uncertainty in the GNSS water vapour product is effectively halved. This validates the "synergistic" approach of using  
 413 collocated MWR thermal data to process GNSS signals.



414  
 415 **Figure 6.** Comparison of weighted mean temperature ( $T_m$ ) derived from HGPT2, MWR, and Radiosonde (RS) during March–November  
 416 2025. (a) Time series of  $T_m$  estimates from all three sources. (b–d) Scatter plots showing statistical comparisons between: (b) HGPT2 vs.  
 417 RS, (c) MWR vs. RS, and (d) HGPT2 vs. MWR.

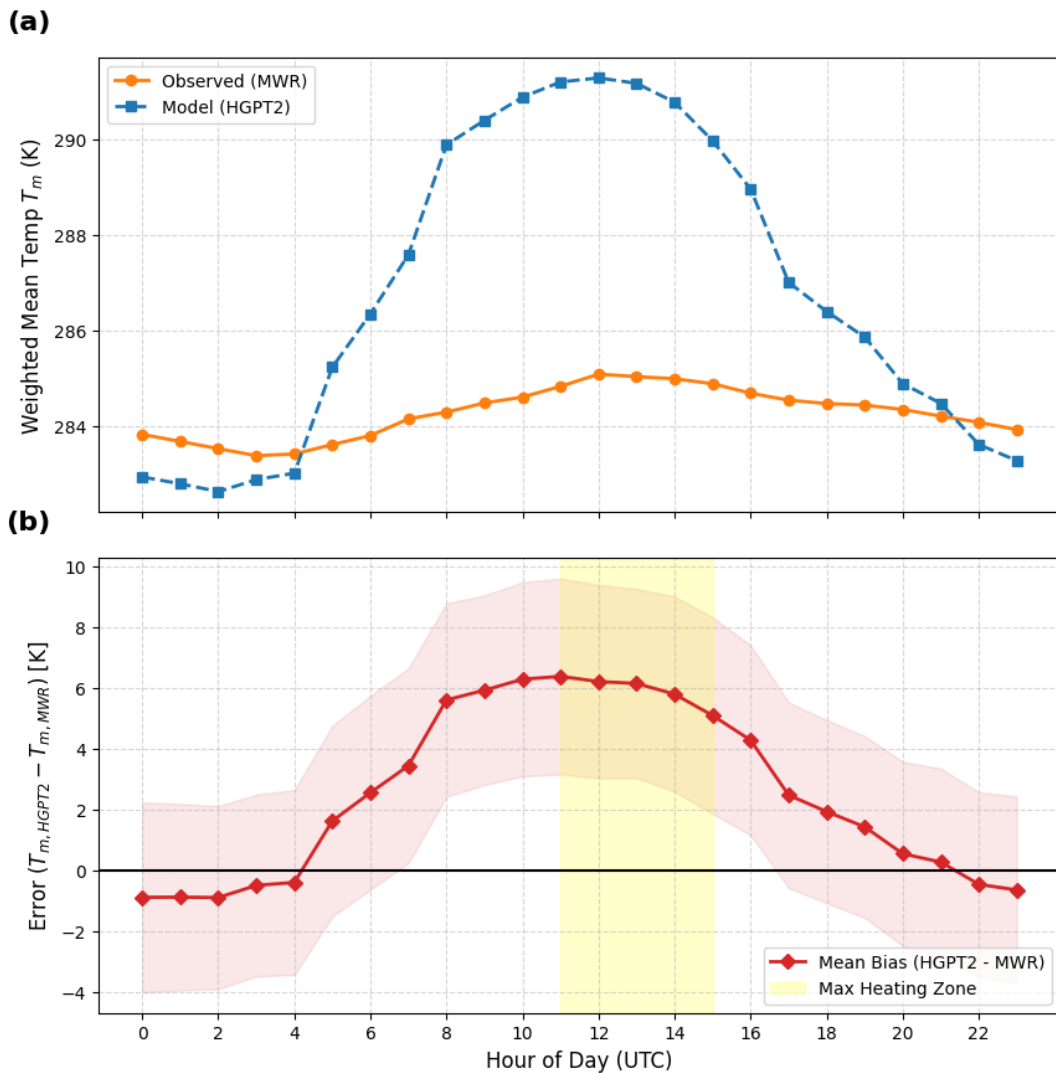
418

## 419 **3.4 Diagnostic Analysis of Thermodynamic Conversion Uncertainty**

### 420 **3.4.1 Diurnal Bias Amplification in Static Models**

421 To pinpoint the physical origin of the HGPT2 model's deficiency, a diurnal cycle analysis was performed (Fig. 7). While the  
422 previous statistical metrics indicated a general positive bias, the temporal breakdown in Fig. 7a reveals that this error is not  
423 uniform, but is driven by a fundamental misrepresentation of atmospheric thermodynamics. The MWR-derived  $T_m$  (orange  
424 line) exhibits a physically realistic, dampened diurnal amplitude of approximately 1.5 K. This stability reflects the high thermal  
425 inertia of the tropospheric column, which does not heat rapidly in response to surface insolation. In stark contrast, the HGPT2  
426 model (blue line) displays an exaggerated diurnal wave with an amplitude exceeding 8.5 K, peaking synchronously with solar  
427 noon (12:00 UTC). As previously documented in the literature (Wang, 2005; Bock, 2021), deriving  $T_m$  via empirical regression  
428 on surface temperature ( $T_s$ ) is known to introduce spurious diurnal cycles. Our observations confirm this intrinsic limitation:  
429 because the empirical model's periodic functions are overly sensitive to  $T_s$ , it assumes intense surface-level heating propagates  
430 uniformly through the column, failing to capture the true thermodynamic decoupling between the turbulent planetary boundary  
431 layer and the stable free troposphere. During the hours of peak solar insolation (11:00–14:00 UTC), the coastal environment  
432 experiences active convective mixing and the onset of the sea breeze, which dramatically alters the vertical distribution of  
433 water vapour. If the underlying reanalysis climatology fails to adequately resolve the sharp moisture capping inversion at the  
434 top of the daytime planetary boundary layer (PBL), it will misrepresent the  $T_m$  weighting function. Specifically, if the model  
435 traps too much moisture near the intensely heated surface—or fails to capture the thermodynamic decoupling between the  
436 turbulent PBL and the stable free troposphere — the integral will disproportionately weight the hottest atmospheric layers.  
437 This coupled temperature-humidity mechanism physically manifests as the severe diurnal bias peak effect observed in Fig. 7b,  
438 where the systematic bias surges to over +6 K. This demonstrates that high-precision GNSS meteorology requires synergistic  
439 MWR data to capture both the true thermal stability and the dynamic vertical moisture weighting of the atmosphere.

440



441  
442  
443  
444  
445

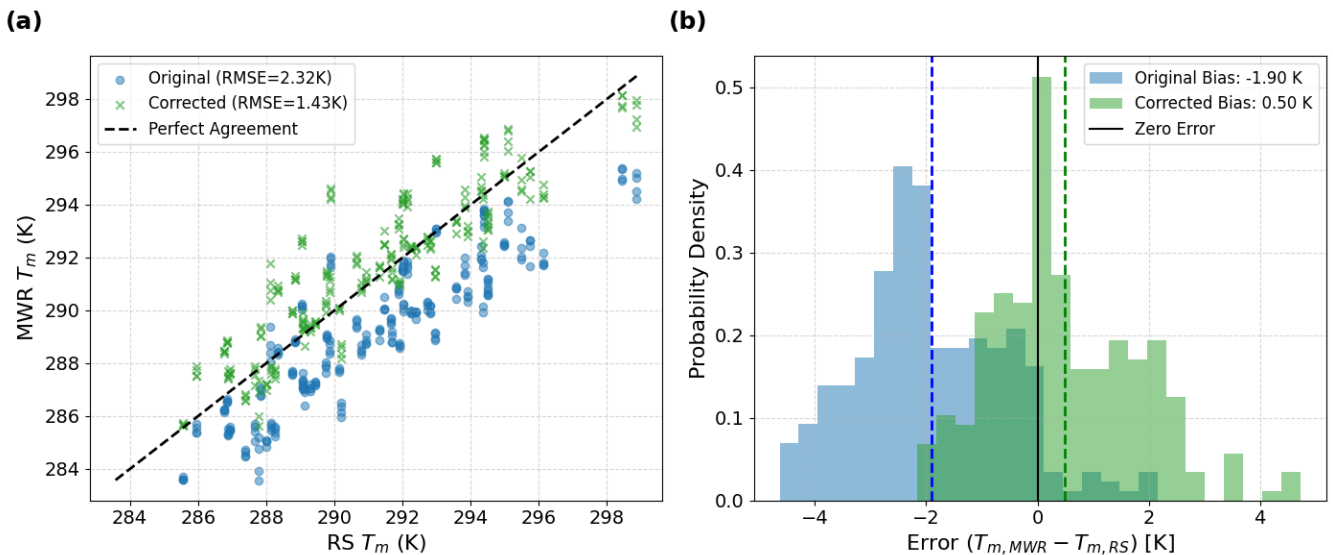
**Figure 7.** Diurnal variation of weighted mean atmospheric temperature  $T_m$  derived from microwave radiometer (MWR) observations and HGPT2 model simulations (top panel). The bottom panel shows the corresponding hourly mean bias ( $T_{m,HGPT2} - T_{m,MWR}$ ), with shaded envelopes indicating variability. The yellow shaded region highlights the period of maximum daytime heating.

### 446 3.4.2 Calibration and Bias Correction of MWR $T_m$

447 Fig. 8 presents a statistical validation of the MWR derived  $T_m$  against co-located RS observations. The analysis highlights the  
448 necessity and efficacy of a linear bias correction scheme to improve GNSS-PWV conversion accuracy. The scatter plot (Fig.  
449 2a) reveals a distinct systematic deviation in the original MWR retrieval relative to the RS reference. The data points  
450 consistently fall below the 1:1 identity line, indicating a negative bias in the raw MWR  $T_m$  product. The original RMSE is 2.32  
451 K. This error is largely driven by the systematic offset rather than random scatter, as evidenced by the high linearity ( $R^2$ ) of

452 the relationship. The thermodynamic profiles were retrieved using the manufacturer's standard Neural Network (NN)  
453 algorithm, trained on Region historical RS data.

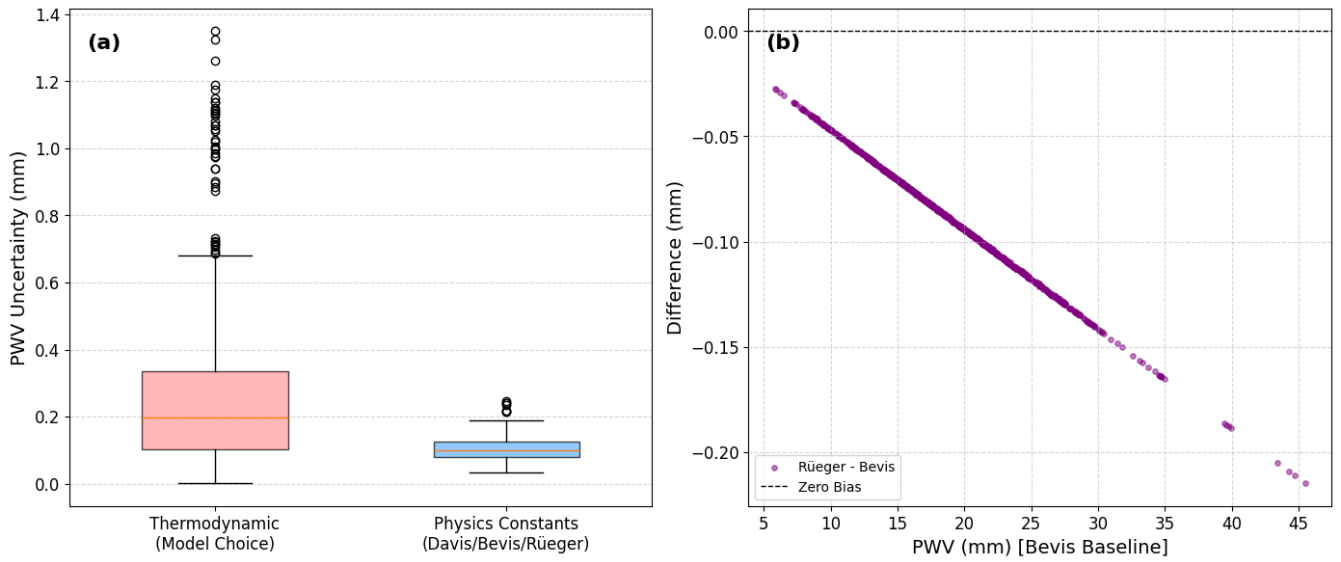
454 The Probability Density Function (PDF) of the errors ( $T_{m,MWR} - T_{m,RS}$ ) in Fig. 8b clearly visualizes the bias shift. The pre-  
455 correction distribution is non-Gaussian and shifted significantly to the negative domain, with a mean bias ( $\mu$ ) of -1.90 K. In  
456 the context of GNSS meteorology, a  $T_m$  error of  $\approx 2$  K translates to a relative PWV error of approximately 0.7–1.0 %. For  
457 climate monitoring, this represents a significant systematic dry bias. Applying the linear correction model (as formulated in  
458 Section 2.2.1) successfully re-centers the error distribution. The post-correction bias is reduced to 0.50 K, and the histogram  
459 aligns symmetrically around the zero-error line. The correction reduces the RMSE to 1.43 K, which is consistent with the  
460 theoretical accuracy limit of ground-based radiometric profiling (typically 1–2 K). The remaining spread (width of the green  
461 histogram) represents the random error component, likely attributable to instrumental noise and the imperfect spatiotemporal  
462 matching between the instantaneous MWR zenith view and the drifting radiosonde balloon. The correction methodology  
463 effectively removes the systematic instrumental bias without artificially compressing the natural variability of the atmosphere.  
464 The reduction of RMSE by  $\sim 38$  % (from 2.32 K to 1.43 K) confirms that site-specific calibration of  $T_m$  is a mandatory  
465 processing step for generating climate-quality GNSS-PWV datasets.



466 **Figure 8.** Evaluation of weighted mean temperature  $T_m$  correction against Radiosonde (RS) observations. (a) scatter plots of original and  
467 bias-corrected MWR-derived  $T_m$  versus RS  $T_m$ , with the dashed line indicating perfect agreement. (b) presents the probability density of  
468 errors ( $T_{m,MWR} - T_{m,RS}$ ) before and after correction, demonstrating a substantial reduction in cold bias and RMSE.  
469  
470

### 471 3.4.3 Uncertainty Budget Analysis

472



473 **Figure 9.** (a) PWV uncertainty attributed to thermodynamic assumptions and to the choice of refractivity constants. (b) Difference in GNSS-  
 474 derived PWV resulting from the use of alternative refractivity constant formulations relative to Bevis et al. (1994).  
 475

476  
 477 In standard GNSS network processing, the largest source of PWV uncertainty is often the interpolation or modeling of  
 478 surface pressure required to calculate the ZHD (Van Malderen et al., 2022). However, the CYGMEN observatory setup  
 479 mitigates this spatial interpolation error by utilizing the co-located Vaisala WXT536 sensor, which has a stated pressure  
 480 accuracy of  $\pm 0.5$  hPa. A 0.5 hPa pressure uncertainty propagates to approximately 1.15 mm of error in the ZHD. After applying  
 481 the  $\Pi$  conversion factor, this restricts the pressure-induced PWV uncertainty to roughly  $\pm 0.17$  mm. Because this high-precision  
 482 localized pressure data effectively minimizes ZHD uncertainty, the accuracy of the  $T_m$  parameterization emerges as the  
 483 dominant remaining variable in the PWV error budget for this site.

484 It is important to note that the complete error budget for GNSS-derived PWV encompasses significant uncertainties  
 485 originating from the ZTD estimation phase itself. These include geodetic errors such as satellite orbit and clock uncertainties,  
 486 mapping function inaccuracies, and site-dependent electromagnetic effects like signal scattering and multipath. While these  
 487 geodetic factors are critical, the following component-wise uncertainty analysis (Fig. 9) specifically isolates the errors  
 488 introduced during the subsequent conversion step ( $\Pi$ ). To decouple these retrieval contributions, two primary sources of  
 489 uncertainty were isolated: the thermodynamic parameterization of  $T_m$  and the selection of atmospheric refractivity constants  
 490 ( $k_2'$ ,  $k_3$ ). When decoupling these retrieval contributions, it is critical to distinguish between the statistical nature of the  
 491 underlying error sources. As demonstrated by Healy (2011), uncertainties in the atmospheric refractivity constants ( $k_2'$ ,  $k_3$ ) act  
 492 strictly as static systematic biases; selecting a different set of published constants permanently shifts the baseline of the  $\Pi$  by  
 493 a fixed margin. Conversely, the uncertainty originating from the  $T_m$  parameterization is a dynamic, compound error. As  
 494 highlighted by Wang et al. (2005) and Bock et al. (2021), empirical  $T_m$  models derived from surface temperatures often fail to

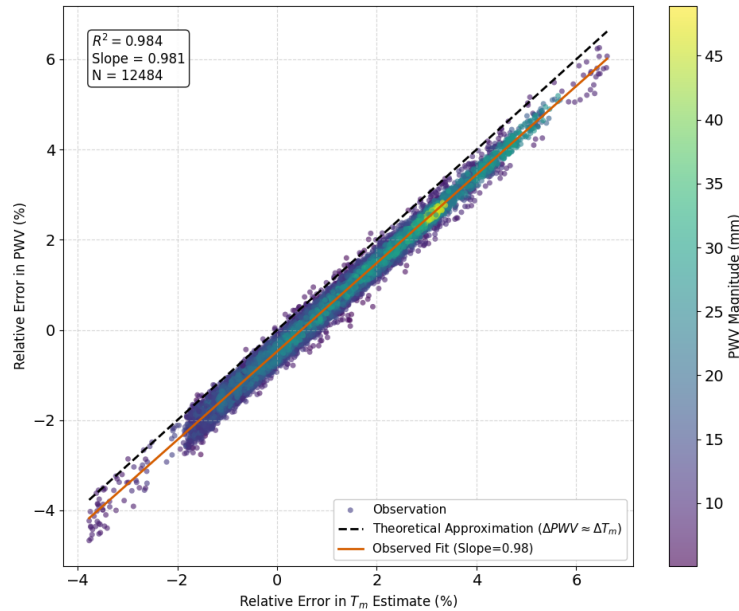
495 capture the true profile variance, introducing both a systematic bias (the model's mean regional offset) and a substantial random  
496 error component (the statistical scatter, or RMSE, driven by real-time thermodynamic variability and diurnal decoupling).  
497 While Fig. 9 juxtaposes these two distinct sources to illustrate their relative bounding magnitude on the final **P**WV product,  
498 their significantly different statistical behaviors—static bias versus dynamic scatter—must be acknowledged. As illustrated in  
499 Fig. 9(a), and explicitly evaluating the components of the conversion uncertainty framework established in Eq. (10), the  
500 variance introduced by the  $T_m$  estimation strategy ( $\sigma_{T_m}^2$ ) significantly outweighs the influence of the physical constants  
501 ( $\sigma_{k_2}^2, \sigma_{k_3}^2$ ). Feeding our empirically derived thermodynamic uncertainties into the partial derivative formulation defined in Eq.  
502 (11) specifically, substituting the HGPT2 RMSE of 4.54 K versus the corrected MWR RMSE of 1.43 K as our  $\sigma_{T_m}$  values—  
503 yields an isolated PWV retrieval error of approximately 1-2 mm due to stochastic thermodynamic variability. In contrast,  
504 evaluating the exact mathematical limits of the refractivity coefficients ( $\sigma_{k_2}, \sigma_{k_3}$ ) defined here as the maximum divergence  
505 between the historical Davis et al. (1985), the standard Bevis et al. (1994), and the updated Rüeiger (2002) formulations—  
506 results in an uncertainty an order of magnitude smaller. Fig. 9(b) further resolves the impact of the refractivity constants,  
507 showing the differential bias between the oldest (Davis) and newest (Rüeiger) standards. The relationship is linear and  
508 proportional to the total water vapour content, consistent with a scaling of the  $\Pi$  factor. While the transition to the Rüeiger  
509 (2002) constants introduces a systematic positive shift, the magnitude of this correction (typically  $<0.2$  mm for standard  
510 loading) is negligible for synoptic meteorological applications compared to the noise induced by  $T_m$  errors. However, for long-  
511 term climatological trend analysis where stability is paramount, consistent adherence to the Rüeiger (2002) standard is  
512 recommended to eliminate this small, but persistent systematic bias. Overall, the correction of the  $T_m$  is 2.5 times more  
513 important than selection of the constant.

514

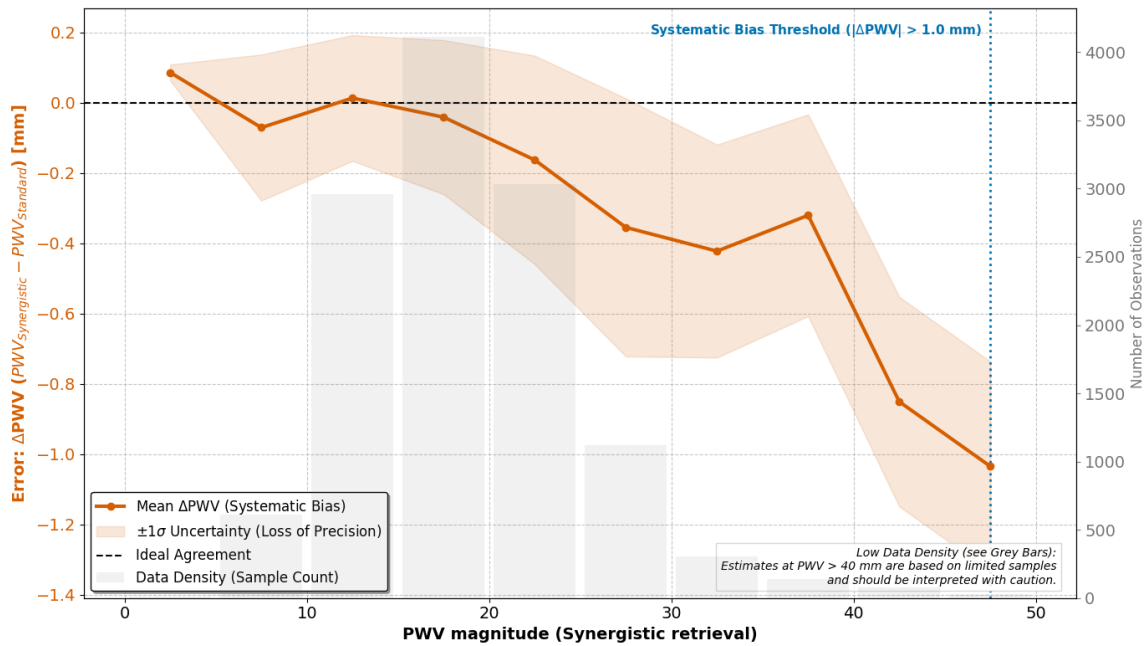
### 515 **3.5 Error Propagation and Synergistic Retrieval Assessment**

516 In this section, the PWV was derived using bias-corrected mean temperature ( $T_m$ ) and constant values based on the study by  
517 Rüeiger (2002), as mentioned in the Sect. 3.4. The impact of  $T_m$  errors on the final PWV product was analyzed to quantify the  
518 benefits of the synergistic retrieval method. Fig. 10 visualizes the direct relationship between the relative error in  $T_m$  and the  
519 resulting relative error in PWV. The plot reveals a strictly linear relationship ( $R^2=0.984$ ) with a slope of 0.981. This confirms  
520 the theoretical approximation that  $(\Delta PWV/PWV) \approx (\Delta T_m/T_m)$ . The color gradient indicates that this linear error propagation  
521 holds true across all PWV magnitudes (from  $<10$  mm to  $>45$  mm). This implies that temperature errors propagate directly into  
522 moisture errors regardless of the humidity level, making accurate  $T_m$  crucial at all times. Fig. 11 investigates the systematic  
523 difference ( $\Delta PWV$ ) between the synergistic retrieval (using MWR  $T_m$ ) and a standard retrieval (using empirical  $T_m$ ) as a function  
524 of moisture abundance (PWV magnitude). For drier conditions (PWV  $< 25$  mm), the difference is minimal (near zero), and  
525 the uncertainty (shaded region) is low. This suggests that for low humidity, the choice of  $T_m$  source is less critical. As  
526 atmospheric moisture increases ( $> 25$  mm), a significant negative bias emerges. The curve dips sharply, reaching nearly  $-1.0$

527 mm at extreme humidity (45+ mm). The 'Systematic Bias Threshold' marker indicates that beyond 45 mm, the discrepancy  
 528 exceeds 1.0 mm. The fact that the bias magnitude scales directly with total PWV provides physical confirmation that the error  
 529 source is located in the boundary layer, where the bulk of the water vapour resides. The growing negative bias demonstrates  
 530 that standard GNSS processing (using static models like HGPT2) systematically overestimates water vapour during extreme  
 531 events compared to the more accurate synergistic method. Rather than extrapolating these localized errors to regional  
 532 hydrological impacts, we emphasize the primary empirical observation: the systemic deviation of the standard empirical model  
 533 scales proportionally with the magnitude of the PWV regime. Crucially, this systematic overestimation of moisture during  
 534 extreme events is deeply intertwined with the diurnal cycle of the local atmosphere. This analysis quantifies the specific  
 535 operational penalty of utilizing static climatological models in this region, demonstrating that HGPT2 incurs an  $\text{PWV}$  error  
 536 exceeding  $1.0 \text{ kg m}^{-3} \text{ mm}$  during severe thermodynamic events. As previously established (Fig. 7), the static HGPT2 model  
 537 displays an exaggerated diurnal wave with an amplitude exceeding 8.5 K. Because the static model fails to account for the  
 538 thermodynamic decoupling between the heated boundary layer and the cooler free troposphere during the day, this  $T_m$  error  
 539 artificially inflates the amplitude of the GNSS-derived PWV diurnal cycle during peak solar insolation. By utilizing the  
 540 synergistic retrieval approach, this spurious daytime moisture amplification is effectively mitigated. While further multi-site,  
 541 long-term studies are required to assess the broader impacts on regional operational forecasting, our localized dataset clearly  
 542 indicates that integrating real-time MWR thermal data successfully removes diurnal artifacts and reduces systematic  
 543 measurement biases at this site.



544 **Figure 10.** Driver of model failure: Impact of weighted mean temperature ( $T_m$ ) accuracy on PWV retrieval.  
 545  
 546  
 547



548  
549  
550

**Figure 11.** Systematic breakdown and instability of the Standard GNSS model under extreme thermodynamic conditions.

#### 551 4 Discussions

552 The results of this study necessitate a fundamental re-evaluation of how  $T_m$  parameterization errors are parameterized in GNSS  
 553 meteorology, particularly within thermodynamically complex, semi-arid coastal environments like the Eastern Mediterranean.  
 554 The pronounced failure of the static HGPT2 model to capture the diurnal  $T_m$  cycle reveals a structural limitation inherent to  
 555 empirical modeling. The observed "diurnal bias peak" effect is not merely a statistical anomaly; it represents a physical  
 556 disconnect. Static empirical models rely heavily on  $T_s$ , effectively assuming that intense surface-level heating propagates  
 557 uniformly through the atmospheric column. This assumption critically breaks down during the daytime in the EM, where the  
 558 turbulent planetary boundary layer (PBL) aggressively decouples from the stable free troposphere. Evidence for this severe  
 559 decoupling is explicitly documented in the high-vertical-resolution RS profiles collected during the campaign. Because the  
 560 passive MWR struggles to effectively capture this sharp boundary—a direct result of the broad weighting functions and  
 561 degraded vertical resolution inherent to its K-band observations—the instrument exhibits a 'smoothing error' across the  
 562 inversion layer. This structural limitation highlights exactly why applying a site-specific bias correction to the MWR's native  
 563 output is a necessary prerequisite for precision GNSS meteorology. Furthermore, the failure of the reanalysis climatology to  
 564 properly resolve the sharp moisture capping inversion during the onset of the daytime sea-breeze significantly corrupts the  
 565 moisture-weighted  $T_m$  integral. Ground-based microwave radiometry overcomes this structural blindness by directly measuring  
 566 the integrated thermal emissions of the column.

567 However, the performance of the MWR in this study highlights the duality of passive microwave remote sensing: it is highly  
568 proficient at retrieving integral quantities but degrades severely when resolving differential or gradient-based parameters. The  
569 successful reduction of the  $T_m$  RMSE via site-specific linear correction confirms that the MWR's K-band and V-band channels  
570 effectively capture the true thermal inertia of the troposphere. The initial systematic cold bias observed aloft is a known artifact  
571 of ill-posed neural network retrievals (Cimini et al., 2006; Löhnert and Maier, 2012). Because the vertical resolution of passive  
572 microwave observations degrades rapidly with height, the retrievals become heavily constrained by historical training datasets  
573 (the climatological prior), which often fail to capture localized, transition-season lapse rates in the free troposphere.  
574 Conversely, the complete failure of the MWR to derive a physically realistic water vapour scale height ( $H_v$ ) exposes the  
575 "smoothing error" inherent to passive radiometry. Because the broad weighting functions of the K-band channels cannot  
576 resolve sharp boundary layer moisture inversions, the retrieval algorithm mathematically smears the moisture mass upward.  
577 This confirms that while MWR serves as a robust standard for total column mass, researchers must exercise extreme caution  
578 when utilizing its smoothed profiles to characterize vertical moisture compactness.

579 While this study relies on a single-site, multi-month dataset, the physical mechanisms identified have broad relevance beyond  
580 the Nicosia region. The Eastern Mediterranean serves as a highly representative climatic hotspot for semi-arid coastal  
581 environments experiencing enhanced warming and intensified hydrological cycles. It is important to note that the specific  
582 threshold of  $>45$  mm identified here is characteristic of the climatological moisture capacity of the Eastern Mediterranean  
583 during extreme summer anomalies. While the exact numerical value of this 'Systematic Bias Threshold' will vary  
584 geographically depending on local atmospheric dynamics and latitude, the underlying physical principle remains universal:  
585 empirical  $T_m$  models systematically degrade proportionally to the total atmospheric moisture mass during severe local  
586 extremes. The core vulnerability exposed in this research—that static global models are structurally blind to sharp boundary  
587 layer thermodynamic decoupling during peak insolation—is a fundamental physics problem, not a local anomaly. Therefore,  
588 the proposed synergistic MWR-GNSS retrieval architecture provides a universally applicable solution for mitigating  
589 systematic dry biases in any complex terrain or coastal environment globally. While the simple linear regression applied in  
590 this study proved highly effective at correcting systematic  $T_m$  biases for operational GNSS conversions, there remains room  
591 for algorithmic improvement. As the CYGMEN infrastructure accumulates a multi-year climatological database of high-  
592 resolution radiosonde profiles, future work should focus on complementary Neural Network (NN) training. By retraining the  
593 MWR retrieval algorithms using site-specific radiative transfer modeling rather than relying on the manufacturer's regional  
594 historical priors, the native temperature and humidity profiles can be further optimized at the retrieval level.

595 Finally, our component-wise uncertainty analysis clarifies the error propagation chain in the GNSS-PWV conversion  
596 process, shifting the paradigm of where optimization efforts should be focused. Historically, significant effort within the  
597 geodetic community has been expended on refining atmospheric refractivity constants. However, we demonstrate that the error  
598 induced by transitioning from the historical Davis et al. (1985) formulations to the modern Rüeiger (2002) constants is

599 practically negligible ( $<0.2$  mm) for synoptic meteorological applications. The true "weak link" in the retrieval chain is  
600 unequivocally the thermodynamic parameterization, which introduces errors an order of magnitude larger.

601

## 602 **5 Conclusion**

603 This study demonstrated that the accuracy of GNSS-derived Precipitable Water Vapour (PWV) in the Eastern Mediterranean  
604 region, is significantly affected by the thermodynamic rigidity of static climatological models. By implementing a synergistic  
605 retrieval strategy that couples GNSS delays with real-time ground-based microwave radiometry (MWR), we successfully  
606 quantified and mitigated these limitations. The investigation yielded three primary methodological conclusions. First, we  
607 established that standard empirical models (e.g., HGPT2) are structurally incapable of resolving the diurnal thermodynamic  
608 decoupling between the boundary layer and free troposphere. This deficiency leads to severe systematic errors (the "diurnal  
609 bias peak" effect) exceeding 6 K in weighted mean temperature ( $T_m$ ) during peak solar insolation, which directly propagates  
610 into a PWV bias  $>1.0$  mm during extreme hygrometric events. Second, the MWR proved to be a superior source for  $T_m$   
611 parameterization errors, provided that site-specific calibration is applied. The development of a linear bias correction scheme  
612 reduced the MWR  $T_m$  root-mean-square error from 2.32 K to 1.43 K. This correction substantially reduces the conversion-  
613 related uncertainty in the GNSS water vapour product compared to standard climatological approaches. Third, the component-  
614 wise sensitivity analysis confirmed that thermodynamic parameterization is a highly significant source of uncertainty that  
615 exacerbates existing geodetic ZTD errors, outweighing uncertainties in refractive index constants by an order of magnitude.  
616 Consequently, the proposed combined retrieval represents a highly valuable architectural upgrade for monitoring severe  
617 weather in complex coastal environments like the Eastern Mediterranean. However, it must be acknowledged that there are  
618 many sites worldwide where the deployment of microwave radiometers may not be justified. Given the high capital and  
619 operational costs of radiometric hardware, the presence of other unmitigated geodetic uncertainties, and the adequate  
620 performance of static  $T_m$  models in less thermodynamically complex regions, this synergistic approach is best reserved for  
621 targeted deployments in highly vulnerable climatic hotspots.

622 For the climate-sensitive Eastern Mediterranean region, relying on static models for GNSS processing risks systematically  
623 masking moisture trends during heatwaves and deep convection. We therefore recommend the operational integration of  
624 collocated MWR observations into national GNSS processing chains. Where collocation is not feasible, future work should  
625 focus on assimilating MWR-derived diurnal shape functions into static models to bridge the gap between climatology and  
626 reality. This study establishes the "Corrected Synergistic Method" as a robust benchmark for generation of climate-quality  
627 water vapour datasets in complex thermodynamic environments. From an operational perspective, relying exclusively on  
628 MWRs for regional moisture monitoring is constrained by high capital costs, maintenance complexity, and signal degradation  
629 during precipitation events. Conversely, GNSS networks provide highly cost-effective, dense, and all-weather monitoring

630 capabilities. The primary operational interest of this proposed methodology is the 'supersite' calibration strategy: utilizing a  
631 centralized MWR to capture the true, real-time thermodynamic diurnal variations that static models like HGPT2 miss, and  
632 subsequently assimilating these dynamic  $T_m$  corrections over a much wider, regional network of standard GNSS receivers.  
633 This synergy allows forecasting centers to leverage the superior thermodynamic accuracy of a single MWR to drastically  
634 improve the high-resolution, continuous PWV datasets generated by dense, low-cost GNSS infrastructure.

### 636 **Data availability**

637 The MWR and GNSS data used in this study are available from the CYGMEN project archive upon request. High resolution  
638 Radiosonde data available from the Department of Meteorology (DoM), Cyprus. The ERA5 reanalysis data can be downloaded  
639 from the Copernicus Climate Change Service (C3S) Climate Data Store.

### 641 **Author contributions**

642 ANP carried out the GNSS, MWR, and Radiosonde data processing, performed the synergistic PWV retrievals and error  
643 diagnosis, and wrote the initial version of the paper. CO and HH conceptualized the study, acquired the funding and resources  
644 for the CYGMEN infrastructure, and supervised the investigation. All authors discussed the results, edited, and proofread the  
645 paper.

### 647 **Competing interests**

648 All authors declare that they have no conflict of interest.

### 650 **Acknowledgements**

651 We would like to express our sincere gratitude to the Cyprus Department of Meteorology (DoM) and in particular to Physicist  
652 and Meteorology Officer Dr. Demetris Charalambous, for his invaluable guidance and for providing access to essential  
653 resources at Athalassa observatory in Nicosia, Cyprus.

655 **Financial support**

656 The present study is funded by the Strategic Infrastructure project CYGMEN, which is implemented in the frames of Cohesion  
657 Policy Programme “THALIA 2021-2027” and is co-funded by the European Union.

658

659 **References**

660 Askne, J. and Nordius, H.: Estimation of tropospheric delay for microwaves from surface weather data, *Radio Sci.*, 22, 379–  
661 386, <https://doi.org/10.1029/RS0221003p00379>, 1987.

662 Bennartz, R. and Bauer, P.: Sensitivity of microwave radiances at 85–183 GHz to precipitating ice particles, *Radio Sci.*, 38,  
663 8075, <https://doi.org/10.1029/2002RS002626>, 2003.

664 Bennett, G. V. and Jupp, A.: Operational assimilation of GPS zenith total delay observations into the Met Office numerical  
665 weather prediction models, *Mon. Weather Rev.*, 140, 2706–2719, <https://doi.org/10.1175/MWR-D-11-00156.1>, 2012.

666 Bevis, M., Businger, S., Herring, T. A., Rocken, C., Anthes, R. A., and Ware, R. H.: GPS meteorology: Remote sensing of  
667 atmospheric water vapor using the Global Positioning System, *J. Geophys. Res.*, 97, 15787–15801,  
668 <https://doi.org/10.1029/92JD01517>, 1992.

669 Bevis, M., Businger, S., Chiswell, S., Herring, T. A., Anthes, R. A., Rocken, C., and Ware, R. H.: GPS meteorology: Mapping  
670 zenith wet delays onto precipitable water, *J. Appl. Meteorol.*, 33, 379–386, [https://doi.org/10.1175/1520-0450\(1994\)033<0379:GMMZWD>2.0.CO;2](https://doi.org/10.1175/1520-0450(1994)033<0379:GMMZWD>2.0.CO;2), 1994.

672 Böhm, J., Möller, G., Schindelegger, M., Pain, G., and Weber, R.: Development of an improved empirical model for slant  
673 delays in the troposphere (GPT2w), *GPS Solut.*, 19, 433–441, <https://doi.org/10.1007/s10291-014-0403-7>, 2015.

674 Bolton, D.: The computation of equivalent potential temperature, *Mon. Weather Rev.*, 108, 1046–1053,  
675 [https://doi.org/10.1175/1520-0493\(1980\)108<1046:TCOEPT>2.0.CO;2](https://doi.org/10.1175/1520-0493(1980)108<1046:TCOEPT>2.0.CO;2) 1980.

676 Brenot, H., Neméghaire, J., Delobbe, L., Clerbaux, N., De Meutter, P., Deckmyn, A., Delcloo, A., Frappez, L., and Van  
677 Roozendael, M.: Preliminary signs of the initiation of deep convection by GNSS, *Atmos. Chem. Phys.*, 13, 5425–5449,  
678 <https://doi.org/10.5194/acp-13-5425-2013>, 2013.

679 Bock, O., Bossler, P., Flamant, C., Doerflinger, E., Jansen, F., Fages, R., Bony, S. and Schnitt, S.: Integrated water vapour  
680 observations in the Caribbean arc from a network of ground-based GNSS receivers during EUREC 4 A. *Earth System Science*  
681 *Data*, 13(5), pp.2407-2436. <https://doi.org/10.5194/essd-13-2407-2021>. 2021.

682 Cimini, D., Westwater, E. R., Gasiewski, A. J., Klein, M., Leuski, V. Y., and Dowlatshahi, S.: Thermodynamic atmospheric  
683 profiling during the 2010 Winter Olympics using ground-based microwave radiometry, *IEEE T. Geosci. Remote*, 49, 4959–  
684 4969, <https://doi.org/10.1109/TGRS.2011.2154337>, 2011.

685 Cimini, Domenico, Tim J. Hewison, Lorenz Martin, Jürgen Güldner, Catherine Gaffard, and Frank S. Marzano. "Temperature  
686 and humidity profile retrievals from ground-based microwave radiometers during TUC." *Meteorologische Zeitschrift* 15, no.  
687 1: 45-56. 2006.

688 Crewell, S. and Löhnert, U.: Accuracy of boundary layer temperature profiles retrieved with multifrequency multiangle  
689 microwave radiometry, *IEEE T. Geosci. Remote*, 45, 2195–2201, doi: 10.1109/TGRS.2006.888434. 2007.

690 Douša, J. and Václavovic, P.: Real-time zenith tropospheric delays in support of numerical weather prediction applications,  
691 *Adv. Space Res.*, 53, 1347–1358, <https://doi.org/10.1016/j.asr.2014.02.021>, 2014.

692 Davis, J. L., Herring, T. A., Shapiro, I. I., Rogers, A. E. E., and Elgered, G.: Geodesy by radio interferometry: Effects of  
693 atmospheric modeling errors on estimates of baseline length, *Radio Sci.*, 20, 1593–1607,  
694 <https://doi.org/10.1029/RS020i006p01593>, 1985.

695 Foth, A., Lochmann, M., Saavedra Garfias, P. and Kalesse-Los, H.: Determination of low-level temperature profiles from  
696 microwave radiometer observations during rain. *Atmospheric Measurement Techniques*, 17(24), pp.7169-7181, 2024.

697 Gaffen, D. J.: Temporal inhomogeneities in radiosonde temperature records, *J. Geophys. Res.*, 99, 3667–3676,  
698 <https://doi.org/10.1029/93JD03179>, 1994.

699 Giannadaki, D., Oikonomou, C., Haralambous, H., Tymvios, F., and Loizou, E.: Validation of precipitable water vapour  
700 products using CyMETEO GNSS network in Cyprus, in: Eleventh International Conference on Remote Sensing and  
701 Geoinformation of the Environment (RSCy2025), Vol. 13816, 397–409, SPIE, 2025.

702 Giorgi, F.: Climate change hot-spots, *Geophys. Res. Lett.*, 33, L08707, <https://doi.org/10.1029/2006GL025734>, 2006

703 Guerova, G., Jones, J., Douša, J., Dick, G., de Haan, S., Pottiaux, E., Bock, O., Pacione, R., Elgered, G., Vedel, H., and Bender,  
704 M.: Review of the state of the art and future prospects of the ground-based GNSS meteorology in Europe, *Atmos. Meas. Tech.*,  
705 9, 5385–5406, <https://doi.org/10.5194/amt-9-5385-2016>, 2016.

706 Held, I. M. and Soden, B. J.: Robust responses of the hydrological cycle to global warming, *J. Climate*, 19, 5686–5699,  
707 <https://doi.org/10.1175/JCLI3990.1>, 2006.

- 708 Healy, S.B.: Refractivity coefficients used in the assimilation of GPS radio occultation measurements. *Journal of Geophysical*  
709 *Research: Atmospheres*, 116(D1). <https://doi.org/10.1029/2010JD014013>. 2011.
- 710 Jiang, P., Ye, S., Chen, D., Liu, Y., and Xia, P.: Development of time-varying global gridded Ts-Tm model for precise GPS-  
711 PWV retrieval, *Atmos. Meas. Tech.*, 12, 1233–1249, <https://doi.org/10.5194/amt-12-1233-2019>, 2019.
- 712 Jones, J., Guerova, G., Douša, J., Dick, G., de Haan, S., Pottiaux, E., Bock, O., Pacione, R., Elgered, G., Vedel, H., and Bender,  
713 M.: Advanced GNSS Tropospheric Products for Monitoring Severe Weather Events and Climate, Springer, Cham,  
714 <https://doi.org/10.1007/978-3-030-13901-8>, 2020.
- 715 Kiehl, J. T. and Trenberth, K. E.: Earth's annual global mean energy budget, *B. Am. Meteorol. Soc.*, 78, 197–208,  
716 [https://doi.org/10.1175/1520-0477\(1997\)078<0197:EAGMEB>2.0.CO;2](https://doi.org/10.1175/1520-0477(1997)078<0197:EAGMEB>2.0.CO;2), 1997.
- 717 Lan, Z., Zhang, B., and Geng, T.: Establishment and analysis of global gridded Tm-Ts relationship model, *Geodesy and*  
718 *Geodynamics*, 7, 101–107, <https://doi.org/10.1016/j.geog.2016.02.001>, 2016.
- 719 Lelieveld, J., Hadjinicolaou, P., Kostopoulou, E., Chenoweth, J., El Maayar, M., Giannakopoulos, C., Hannides, C., Lange,  
720 M. A., Tanarhte, M., Tyrllis, E., and Xoplaki, E.: Climate change and impacts in the Eastern Mediterranean and the Middle  
721 East, *Climatic Change*, 114, 667–687, <https://doi.org/10.1007/s10584-012-0418-4>, 2012.
- 722 Li, H., Wang, X., Wu, S., Zhang, K., Chen, X., Qiu, C., Zhang, Q., and Li, L.: Development of an improved model for  
723 prediction of short-term heavy precipitation based on GNSS-derived PWV, *Remote Sens.*, 12, 4101,  
724 <https://doi.org/10.3390/rs12244101>, 2020.
- 725 Löhnert, U. and Maier, O.: Operational profiling of temperature using ground-based microwave radiometry at Payerne:  
726 Prospects and challenges, *Atmos. Meas. Tech.*, 5, 1121–1134, <https://doi.org/10.5194/amt-5-1121-2012>, 2012.
- 727 Mateus, P., Mendes, V. B., and Plecha, S. M.: HGPT2: an ERA5-based global model to estimate relative humidity, *Remote*  
728 *Sens.*, 13, 2179, <https://doi.org/10.3390/rs13112179>, 2021.
- 729 Ning, T. and Elgered, G.: Intercomparison of MAX-DOAS vertical profile retrieval algorithms: studies on field data from the  
730 CINDI-2 campaign, *Atmos. Meas. Tech.*, 14, 1–35, <https://doi.org/10.5194/amt-14-1-2021>, 2021.
- 731 Ning, Tong, J. Wang, G. Elgered, G. Dick, J. Wickert, Markus Bradke, M. Sommer, R. Querel, and D. Smale. "The uncertainty  
732 of the atmospheric integrated water vapour estimated from GNSS observations." *Atmospheric Measurement Techniques* 9, no.  
733 1. 79-92. doi:10.5194/amt-9-79-2016. 2016.

734 Pakkattil, A., Parde, A. N., Wagh, S., Lonkar, P., and Ghude, S. D.: Wintertime Intercomparison of Specific Humidity and  
735 Temperature Profiles Measured by Microwave Radiometer (MWR), Radiosonde, and INSAT-3DR Sounder Over Delhi, India,  
736 *J. Geophys. Res. Atmos.*, 130, e2025JD044462, <https://doi.org/10.1029/2025JD044462>, 2025.

737 Parde, A. N., Ghude, S. D., Prasad, V. S., Hari Prasad, K. B. R. R., Dhargar, N. G., Lonkar, P., and Rajeevan, M.: Influence  
738 of ground-based microwave radiometer profile assimilation on fog genesis forecasts in the winter boundary layer of Northern  
739 India, *J. Geophys. Res. Atmos.*, 130, e2024JD042224, <https://doi.org/10.1029/2024JD042224>, 2025.

740 Oikonomou, C., Tymvios, F., Pikridas, C., Bitharis, S., Balidakis, K., Michaelides, S., ... and Charalambous, D.: Tropospheric  
741 delay performance for GNSS integrated water vapor estimation by using GPT2w model, ECMWF's IFS operational model and  
742 in situ meteorological data, *Adv. Geosci.*, 45, 363–375, <https://doi.org/10.5194/adgeo-45-363-2018>, 2018.

743 Realini, E., Gatti, A., Reguzzoni, M., Sampietro, D., and Venuti, G.: GNSS-based precipitable water vapor retrieval for severe  
744 weather monitoring: The 2014 Genoa flood case study, *Adv. Space Res.*, 53, 1–10, <https://doi.org/10.1016/j.asr.2014.02.015>,  
745 2014.

746 Rüeiger, J. M.: Refractive index formulae for radio waves, in: Proceedings of the FIG XXII International Congress,  
747 Washington, D.C., USA, 19–26 April 2002, 1–13, 2002.

748 Ross, R. J. and Elliott, W. P.: Tropospheric water vapor climatology and trends over North America: 1973–93, *J. Climate*, 9,  
749 3561–3574, [https://doi.org/10.1175/1520-0442\(1996\)009<3561:TWVCAT>2.0.CO;2](https://doi.org/10.1175/1520-0442(1996)009<3561:TWVCAT>2.0.CO;2). 1996.

750 Saastamoinen, J.: Atmospheric correction for the troposphere and stratosphere in radio ranging satellites, in: The Use of  
751 Artificial Satellites for Geodesy, *Geophys. Monogr. Ser.*, 15, 247–251, AGU, Washington, D.C.,  
752 <https://doi.org/10.1029/GM015p0247>, 1972.

753 Soden, B. J. and Lanzante, J. R.: An assessment of satellite and radiosonde climatologies of upper-tropospheric water vapor,  
754 *J. Climate*, 9, 1235–1250, [https://doi.org/10.1175/1520-0442\(1996\)009<1235:AAOSAR>2.0.CO;2](https://doi.org/10.1175/1520-0442(1996)009<1235:AAOSAR>2.0.CO;2), 1996.

755 Steinke, S., Ebell, K., Löhnert, U., Bozzo, A., Crewell, S., and Turner, D. D.: Assessment of small-scale integrated water  
756 vapour variability during HOPE, *Atmos. Chem. Phys.*, 15, 2675–2692, <https://doi.org/10.5194/acp-15-2675-2015>, 2015.

757 Thayer, G. D.: An improved equation for the radio refractive index of air, *Radio Sci.*, 9, 803–807,  
758 <https://doi.org/10.1029/RS009i010p00803>, 1974.

759 Trenberth, K. E., Fasullo, J., and Smith, L.: Trends and variability in column-integrated atmospheric water vapor, *Clim.*  
760 *Dynam.*, 24, 741–758, <https://doi.org/10.1007/s00382-005-0017-4>, 2005.

- 761 Van Malderen, R., Brenot, H., Pottiaux, E., Beirle, S., Hermans, C., De Mazière, M., ... and Bruyninx, C.: A multi-site  
762 intercomparison of integrated water vapour observations for climate change analysis, *Atmos. Meas. Tech.*, 7, 2487–2512,  
763 <https://doi.org/10.5194/amt-7-2487-2014>, 2014.
- 764 ~~[Van Malderen, R., Pottiaux, E., Stankunavicius, G., Beirle, S., Wagner, T., Brenot, H., Bruyninx, C. and Jones, J.: Global](#)~~  
765 ~~[spatiotemporal variability of integrated water vapor derived from GPS, GOME/SCIAMACHY and ERA-Interim: Annual](#)~~  
766 ~~[cycle, frequency distribution and linear trends. \*Remote Sensing\*, 14\(4\), p.1050, <https://doi.org/10.3390/rs14041050>, Van](#)~~  
767 ~~[Malderen, R., Pottiaux, E., Stankunavicius, G., Beirle, S., Wagner, T., Brenot, H., Bruyninx, C., and Jones, J.: Global](#)~~  
768 ~~[Spatiotemporal Variability of Integrated Water Vapor Derived from GPS, GOME/SCIAMACHY and ERA-Interim: Annual](#)~~  
769 ~~[Cycle, Frequency Distribution and Linear Trends. \*Remote Sens.\*, 14, 1050, <https://doi.org/10.3390/rs14041050>, 2022.](#)~~
- 770 Van Baelen, J., Aubagnac, J.P. and Dabas, A.: Comparison of near–real time estimates of integrated water vapor derived with  
771 GPS, radiosondes, and microwave radiometer. *Journal of Atmospheric and Oceanic Technology*, 22(2), pp.201-210, 2005.
- 772 Vaquero-Martínez, J., Antón, M., Ortiz de Galisteo, J. P., Cachorro, V. E., Wang, H., González-Abad, G., ... and Costa, M. J.:  
773 Inter-comparison of integrated water vapor from ground-based GPS and satellite remote sensing at Mediterranean sites, *IEEE*  
774 *J. Sel. Top. Appl.*, 11, 1718–1728, <https://doi.org/10.1109/JSTARS.2018.2812804>, 2018.
- 775 Ware, R., Cimini, D., Herzegh, P., Marzano, F., Vivekanandan, J. and Westwater, E.: Ground-based microwave radiometer  
776 measurements during precipitation. In *8th Specialist Meeting on Microwave Radiometry* (pp. 24-27), 2004.
- 777 Wang, Junhong, Liangying Zhang, and Aiguo Dai. "Global estimates of water-vapor-weighted mean temperature of the  
778 atmosphere for GPS applications." *Journal of Geophysical Research: Atmospheres* 110, no. D21. doi:10.1029/2005JD006215.  
779 2005.
- 780 Yao, Y., Zhang, B., Yue, S., Xu, C., and Peng, W.: Analysis of the global Tm-Ts correlation and establishment of the latitude-  
781 related linear model, *Chin. Sci. Bull.*, 59, 2340–2347, <https://doi.org/10.1007/s11434-014-0275-9>, 2014.
- 782 Ziskin Ziv, S., Yair, Y., Alpert, P., Uzan, L., and Reuveni, Y.: The diurnal variability of precipitable water vapor derived from  
783 GPS tropospheric path delays over the Eastern Mediterranean, *Atmos. Res.*, 249, 105307,  
784 <https://doi.org/10.1016/j.atmosres.2020.105307>, 2021.
- 785 Ziskin Ziv, S., Alpert, P., and Reuveni, Y.: Long-term variability and trends of precipitable water vapour derived from GPS  
786 tropospheric path delays over the Eastern Mediterranean, *Int. J. Climatol.*, 41, 6433–6454, <https://doi.org/10.1002/joc.7205>,  
787 2021.

788 Zittis, G., Hadjinicolaou, P., Klangidou, M., et al.: A multi-model, multi-scenario, and multi-domain analysis of regional  
789 climate projections for the Mediterranean, *Reg. Environ. Change*, 19, 2621–2635, <https://doi.org/10.1007/s10113-019-01565->  
790 w, 2019.